HIGH FREQUENCY CONSTRAINTS ON THE LAYOUT OF WIDE BAND GAP-BASED POWER ELECTRONIC ASSEMBLIES WITHIN SHIELDED ENCLOSURES

by

Jonathan H. Itokazu

A Thesis Submitted in

Partial Fulfillment of the

Requirements for the Degree of

Master of Science

in Engineering

at

The University of Wisconsin-Milwaukee

May 2019

ABSTRACT

HIGH FREQUENCY CONSTRAINTS ON THE LAYOUT OF WIDE BAND GAP-BASED POWER ELECTRONIC ASSEMBLIES WITHIN SHIELDED ENCLOSURES

by

Jonathan H. Itokazu

The University of Wisconsin-Milwaukee, 2019
Under the Supervision of Professor Robert Cuzner

Since its integration into power electronic converters, the value proposition of wide band gap semiconductors has yet to be holistically realized due to the high frequency effects associated with increased switching speeds. The United States Navy's Smart Ship System Design (S3D) platform enables the investigation of wide band gap-based devices in shipboard Medium Voltage Direct Current (MVDC) Integrated Power and Energy Systems (IPES) through the use of metaheuristic model-based scaling laws. These physics-based scaling laws are produced from a virtual prototyping approach which takes into account the discrete building blocks associated with multi-cell based power conversion and distribution equipment and can be used to predict size, weight, losses, cost and reliability. In present practice, the discrete building blocks consist of power electronic assemblies laid out and enclosed within shielded enclosures. In an effort to incorporate the high frequency effects associated wide band gap-based Power Electronic Building Blocks (PEBB) into the virtual prototyping approach, a mathematical model which captures the high frequency effects is formulated in this thesis.

TABLE OF CONTENTS

LIST OF FIGURES

LIST OF TABLES

Chapter 1

Introduction

Power electronic converters convert electric power from one type to another through various switching schemes. The silicon (Si)-based semiconductor switching devices in the converter are controlled on or off at various intervals, allowing voltages and currents can be converted from AC to DC, DC to AC, AC to AC, or DC to DC; making power electronic converters an essential part of power distribution systems. As power conversion equipment, converters need to be highly efficient and reliable in addition to meeting performance requirements. For shipboard power systems, converters should also be as power dense as possible in order to maximize space and the use of fuel. In order to achieve these goals, significant developments in Si power semiconductor technology have been achieved over past the 50 years.

Despite present day Si-based power converters being highly efficient, with efficiencies up to as high as 98%, they are not as efficient as traditional electromagnetic converters [1]. The relatively high loss and limited switching speed of Si devices introduces heat and switching ripples, necessitating the implementation of cooling systems and passive components for waveform smoothing and filtering, thus limiting further improvements towards higher power density. With shipboard power demands steadily rising, system currents are reaching the limits of electromechanical switchgears and breakers, thus necessitating higher system voltages to manage current levels. Additionally, transformers and filters are very heavy and bulky, but their size and weight can be dramatically reduced by increasing operating and switching frequencies.

Current Si power semiconductor devices, namely the Si Insulated Gate Bipolar Transistor (IGBT), are approaching material theoretical limitations in regards to voltage blocking capabilities, operation temperature, and conduction and switching performance. The highest voltage rating commercially available is 6.5 kV and there are no commercial Si-based devices with junction temperature capability above 175 °C [1, 2]. These intrinsic limitations become a barrier to improve power converters further, however, the emergence of Wide-Bandgap (WBG) power semiconductor devices promises to revolutionize power electronic converters by remedying these limitations.

1.1 Wide Band Gap Power Semiconductors

A comparison of the characteristics between Si and WBG semiconductors is summarized in the figure below [3].

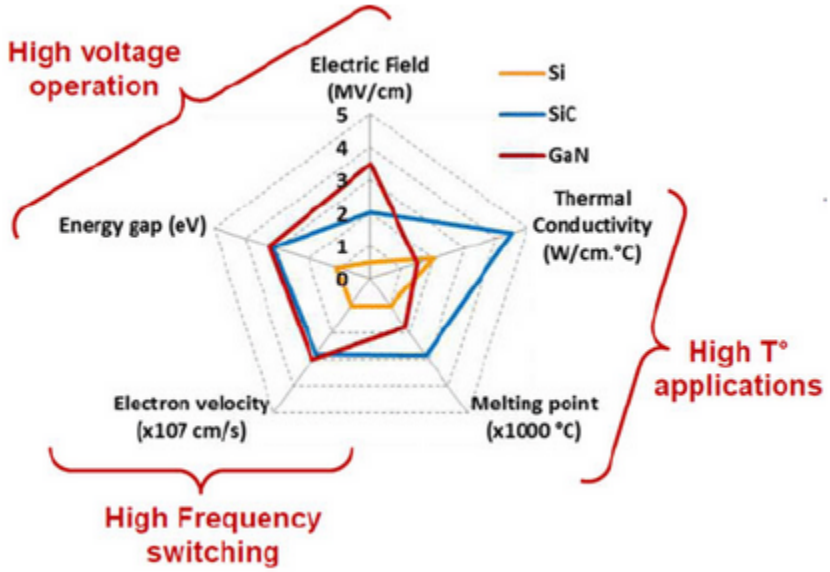

Fig. 1.1: Summary of Si, SiC, and GaN relevant material properties [3]

The two semiconductor materials of interest for power applications are Gallium Nitride (GaN) and Silicon Carbide (SiC). Although GaN offers better high-frequency and high-voltage performances, the lack of availability of good-quality bulk substrates and its lower thermal conductivity make SiC better suited for medium and high voltage applications [4]

and will be the main focus on this work.

In comparison to Si, the higher critical electric field of SiC allows for higher blocking voltages for a given thickness. Alternatively, the higher electric field enables a thinner drift layer with a higher doping concentration to be used for WBG power devices at the same blocking voltage and leads to a lower on-state resistance, resulting in a reduction in switching losses, and a reduction in chip area. This reduction in size also results in a decrease in the junction capacitance which allows for fast switching capability. Furthermore, the electron velocity is, which a measure of carriers being swept out of the depletion region during a turn-off transient, is significantly higher than that of Si, which also leads to an increased switching speed. The thermal conductivity of SiC allows WBG devices to dissipate heat much more efficiently than Si devices. As a result, WBG devices can handle larger amounts of power at a given junction temperature.

The benefits of WBG devices in shipboard electric power systems can be realized primarily in four ways. The first of which is the substitution of Si PIN diodes with SiC Schottky diodes, this alone can lead to a reduction in switching losses and cooling requirements due to the superior reverse recovery characteristics of SiC Schottky diodes [5]. Second is the substitution of Si active switches with WBG devices which has the potential to lead to lower active switching loss, reduced cooling requirements, and smaller passive components which directly impacts efficiency, power density, and temperature capabilities of the converter. The third realization is the impact of the high-voltage and high-frequency capabilities of WBG devices on converter topologies. The use of WBG devices enables simpler topologies to be employed while achieving the same functionality and performance of more complex topologies employed by Si devices, thus enabling the amount of passive components and their size to be reduced. The fourth realization is the modification of system level configurations which are enabled by WBG device characteristics. In shipboard systems, an example of this realization can be seen when considering how the fast switching capabilities of WBG devices can enable high-speed motor drives, thus reducing motor size and yielding higher power density, smaller footprints, and potentially lower system cost [1].

1.2 High Frequency Effects of WBG

The benefits of WBG devices do not come without fault. Much of the performance benefit gained from WBG devices is attributed to their increased switching speeds (dv/dt, di/dt), which in turn increases the generation of Electromagnetic Interference (EMI), due to stray capacitances and inductances in interconnections, and cables [6, 7], with spectral content in the previously un-encountered range of 10-100 MHz [6, 8, 9].

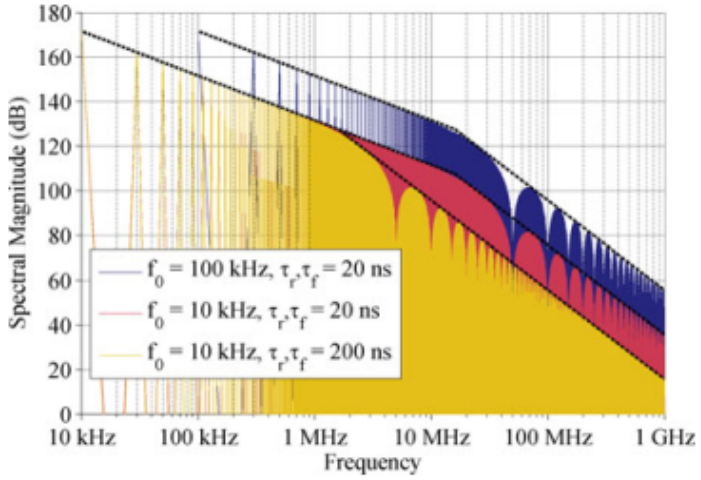

Fig. 1.2: Spectra of trapezoidal waveforms with different fundamental frequencies and rise/fall times[8]

Figure 1.2 shows the magnitude spectra and spectral envelopes of three symmetrical trapezoidal waveforms having the same amplitude and duty cycle, but different fundamental switching frequencies f_0 and rise/fall times, τ_r and τ_f indicated in the figure. The yellow, red, and blue waveforms are representative of present IGBT technology, direct replacement of IGBTs with SiC-based devices, and a significant increase in switching frequency using SiC-based devices, respectively. The investigation in [8] carried out by Oswald *et al.* showed that an order-of-magnitude reduction in switching losses can be obtained by exploiting the full switching-speed capability of SiC based devices. However, this reduction comes at the cost of a 20-30 dB increase in the high-frequency spectral content and a 5-fold node increase in switching node dv/dt. It is also noted in [8] that if the devices are operated at switching speeds significantly lower than what they are capable of, a reduction in switching losses of

50%-75% are obtainable while meeting EMI requirements by the same methods employed in IGBT-based drives. While this reduction is switching losses leads to a reduction in volume of cooling systems, the promises of increased power density and efficiency offered from SiC devices are not realized.

1.3 Thesis Objective

Present research efforts are directed towards addressing these issues at the device level [10–12], however, the value of WBG devices at the system level have yet to be fully realized and understood due to the complexities of the interactions between subsystems and high frequency effects of WBG devices. Effective implementations of medium voltage power conversion systems consist of Lowest Replaceable Units (LRUs) which enable voltage and power scalable systems. LRUs are comprised Power Electronic Building Blocks (PEBBs), EMI filters, passive components, etc. arranged and interconnected within an enclosure.

Following the methodology proposed in [13], the LRUs undergo a Virtual Prototyping Process (VPP) which incorporates a Multi-Objective Optimization (MOO), ensuring Pareto optimized solutions against multiple objectives, and results in obtaining physics-based scaling laws. These scaling laws will predict size, weight, losses, cost and reliability as a function of design space variables such as voltage, frequency, power levels, topological choices, etc. With the wavelengths of the spectral content approaching the vicinity of the enclosure dimensions, it becomes important to incorporate models which take into account radiated EMI behavior into the VPP. This work aims to develop the framework which informs the VPP of the high frequency effects incurred from WBG devices by outlining potential constraints, design space variables, and optimization objectives from the perspective of radiated EMI.

THIS PAGE INTENTIONALLY LEFT BLANK

Chapter 2

Multi-Objective Optimization

To support early concept explorations on ship system designs from electrical, mechanical, thermal and layout standpoints, the United States Navy has developed the Smart Ship System Design (S3D). S3D is a platform that combines multiple disciplines of engineering and areas of physics with a three dimensional ship design and arrangement layout environment. By incorporating scalable models of WBG power conversion and distribution equipment into S3D, naval architects should be able to understand the value proposition of WBG devices into their ship designs. These models should be capable of exploring various topological implementations for a given power conversion or distribution function, as well as show how equipment scales in size, weight, efficiency, etc. with choice of topology.

This work is built around the methodology proposed by Cuzner *et al.* in [13, 14], which produces meta-heuristic model (metamodel)-based scaling laws from a virtual prototyping approach that takes into account the discrete building blocks associated with multi-cell based power conversion and distribution equipment. This approach is aimed at developing scalable modules for the Leading Edge Architecture for Protoyping Systems (LEAPS) database, which serves as a catalog of equipment for S3D, and is optimized to one of five selectable objectives within S3D: power density(ρ); specific power(γ); efficiency(η); reliability(λ^{-1}); or specific cost(σ). While metamodels for scalable electromagnetic energy conversion devices, such as generators and motors, have already been introduced into the

S3D environment [15, 16] the development of metamodels for power conversion and distribution equipment faces difficulties due to the multidisciplinary nature of power electronic-based system designs, the strong influence of cabinet structure and accessibility on power density as the equipment scales up in size, and the need to incorporate power electronic system implementations into enclosures that mitigate the impact of the power electronics on the surrounding thermal and Electromagnetic Compatibility (EMC) of the environment. This chapter is dedicated to providing an overview of the shipboard module ontology, the metamodeling approach, and the VPP, which takes place within the metamodeling approach, that this works work aims to inform.

2.1 Shipboard Module Ontology

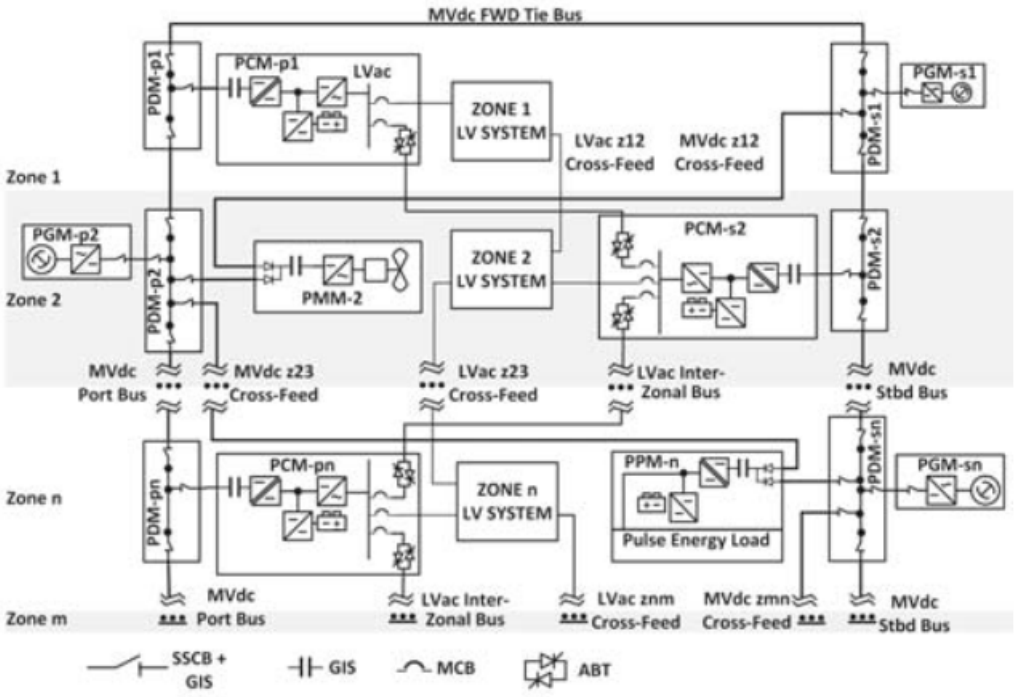

Fig. 2.1: Notional Integrated Energy and Power System [17]

For shipboard power systems, Integrated Energy and Power System (IPES)-based electrical architectures are used for their ability to be re-configurable. In an IPES based architecture, all power and energy flows from generational sources and energy storage devices through

power electronic-based modules. The modules which make up the notional IPES architecture shown above in Figure 2.1 consists of a Power Generation Module (PGM), which converts chemical energy to Medium Voltage Direct Current (MVDC) electrical energy; a Power Conversion Module (PCM), which converts MVDC electrical energy to inter-zonal Low Voltage Direct Current (LVDC) distribution systems; a Power Distribution Module (PDM), which longitudinally distributes zonal MVDC power and energy; a Propulsion Motor Module (PMM), which converts MVDC electrical energy to mechanical propulsion energy; and a Pulsed Power Module (PMM), which converts MVDC electrical energy to projectile or directed energy for energy-based weaponry.

From a dimensional perspective, the physical layout of the module can be sub-divided into either cylindrical structures, such as turbines, generators, or motors, and rectangular structures. Scalable metamodels for cylindrical structures already exist within S3D [17], thus the metamodeling approach referenced within this work aims to develop scalable metamodels for implementation within S3D. The rectangular structures will scale in an ontological structure which organizes LRUs into drawers, multiple drawers into compartments, which are then organized into bays as depicted in Figure 2.2.

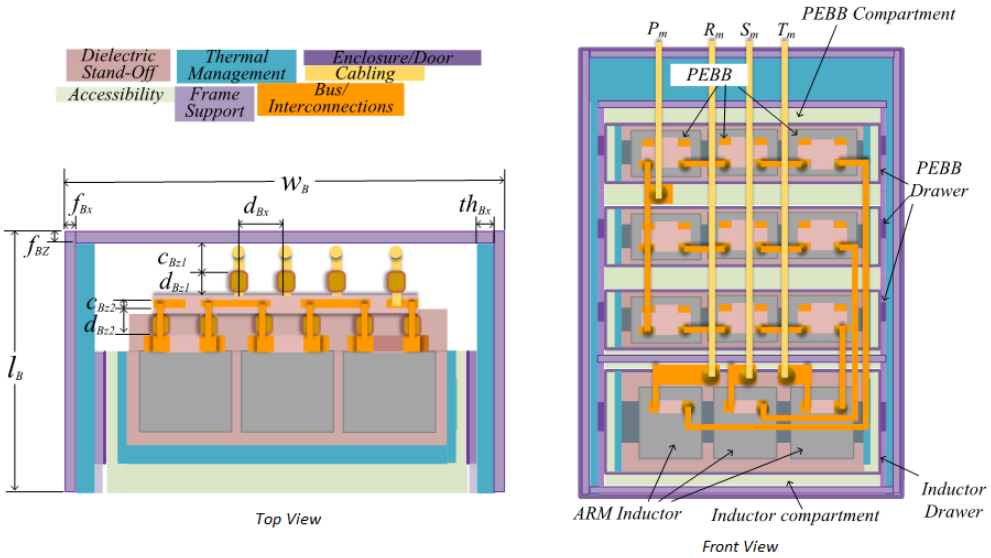

Fig. 2.2: Top (left) and front (right) view of a Modular Multi-level Converter arranged into a bay

The bay serves as the fundamental building block for module scaling and is optimized to a specific objective such as minimum size, weight or cost, or maximum efficiency or reliability. The size and weight of the bay is built up from PEBB and inductor LRU types arranged in drawers, which are arranged optimally within compartments based on given height constraints, which are arranged into the bay with each level having allocations for dielectric stand-off, thermal management, frame and paneling structure, accessibility, and cable and bus interconnections.

2.2 Metamodel Generation Process

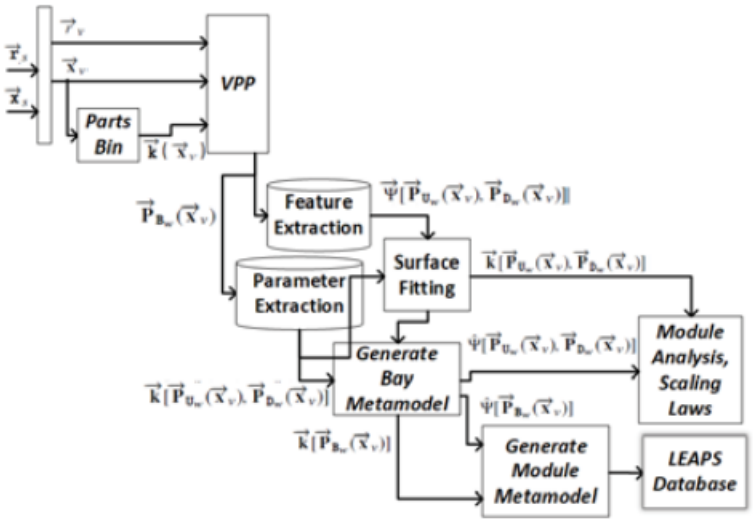

Fig. 2.3: Overview of metamodel generation process [17]

An overview of the metamodel generation process is shown above. The VPP, which will be discussed in the following subsection, receives subsets $\mathbf{r}_\nu$ and $\mathbf{x}_\nu$ of the shipboard design constraints $\mathbf{r}_s$ and design space $\mathbf{x}_s$ as its inputs. The design space consists of a range of design variables, which serve as the building blocks of the design. Examples of design variables would be various PEBB types, ambient operating temperatures, voltage levels, operating frequencies, etc.

The output of the VPP is a $\rho - \gamma - \eta - \lambda^{-1} - \sigma$ Pareto optimized feature space of the bay and results in total of $5 \cdot N$ design, where N is the number of possible meaningful combination of the design space variables. For example, if a design space consisted of

$$Ptype = \{PEBB\,1000,\ PEBB\,6000\}$$
$$\langle v_d \rangle = \{12\,\text{kV},\ 18\,\text{kV},\ 24\,\text{kV}\}$$
$$f_e = \{60\,\text{Hz},\ 120\,\text{Hz},\ 180\,\text{Hz}\},$$

every meaningful combination would enter this process as a subset, i.e., a single design. Then for a particular subset, e.g., $\mathbf{x}_\nu = \{PEBB\,6000,\ 18\,\text{kV},\ 180\,\text{Hz}\}$, entering the generation process results in 5 designs, each optimized to one of the objectives.

The LRU and Drawer performance features, e.g., LRU stresses, drawer level losses, pressure drop, temperature increase, etc., and the parameters associated with the Pareto front of the performance space, e.g., drawer dimensions and weight, are then extracted through the feature and parameter extraction blocks and mapped back to the VPP design space inputs $\mathbf{x}_\nu$. The surface fitting block performs least square surface fitting of the LRU and Drawer performance features so that behavior models can be derived as a function of those subsets $\mathbf{x}_\nu$ which will form dynamic module interfaces.

The metamodel data is then constructed from these inputs and is used to create a metamodel that is a function of module design space inputs and performance versus design space. This metamodel is then programmed into the LEAPS database. The metamodel generation process also analyzes the the Pareto front performance space and functions in order to produce metrics for performance as a function of design space changes. From the surface fitting block, scaling laws which estimate the impacts of design changes on future metrics can be derived by including least square curve fitting to the parameter surfaces, enabling the entire process to provide insight on the impacts of inserting emerging technologies into shipboard equipment.

2.3 Virtual Prototyping Process

The main objective of the virtual prototyping process within the metamodel generation process is to obtain an optimal system design for the cabinet base of the ship. Figure 2.4 shows the overall VPP which takes place within the metamodel generation process depicted in Figure 2.3.

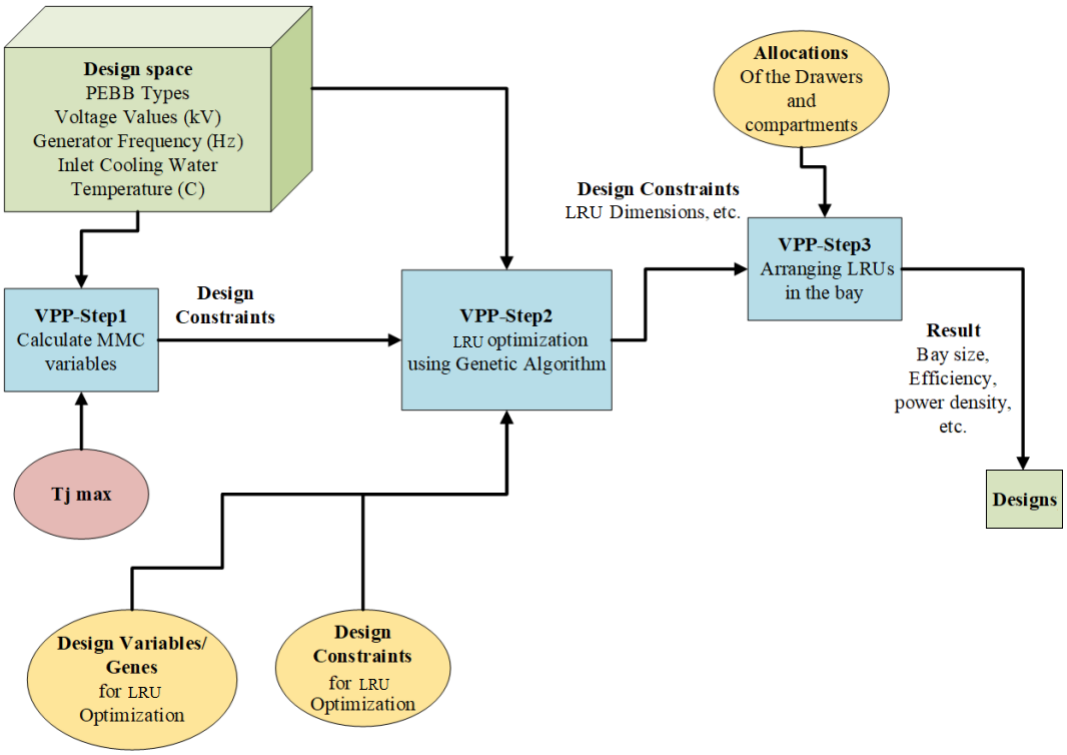

Fig. 2.4: Overall virtual prototyping process [18]

Design variables enter the first step of the VPP which calculates dependent variables from the system model and design constraints according to the flowchart shown below in Figure 2.5.

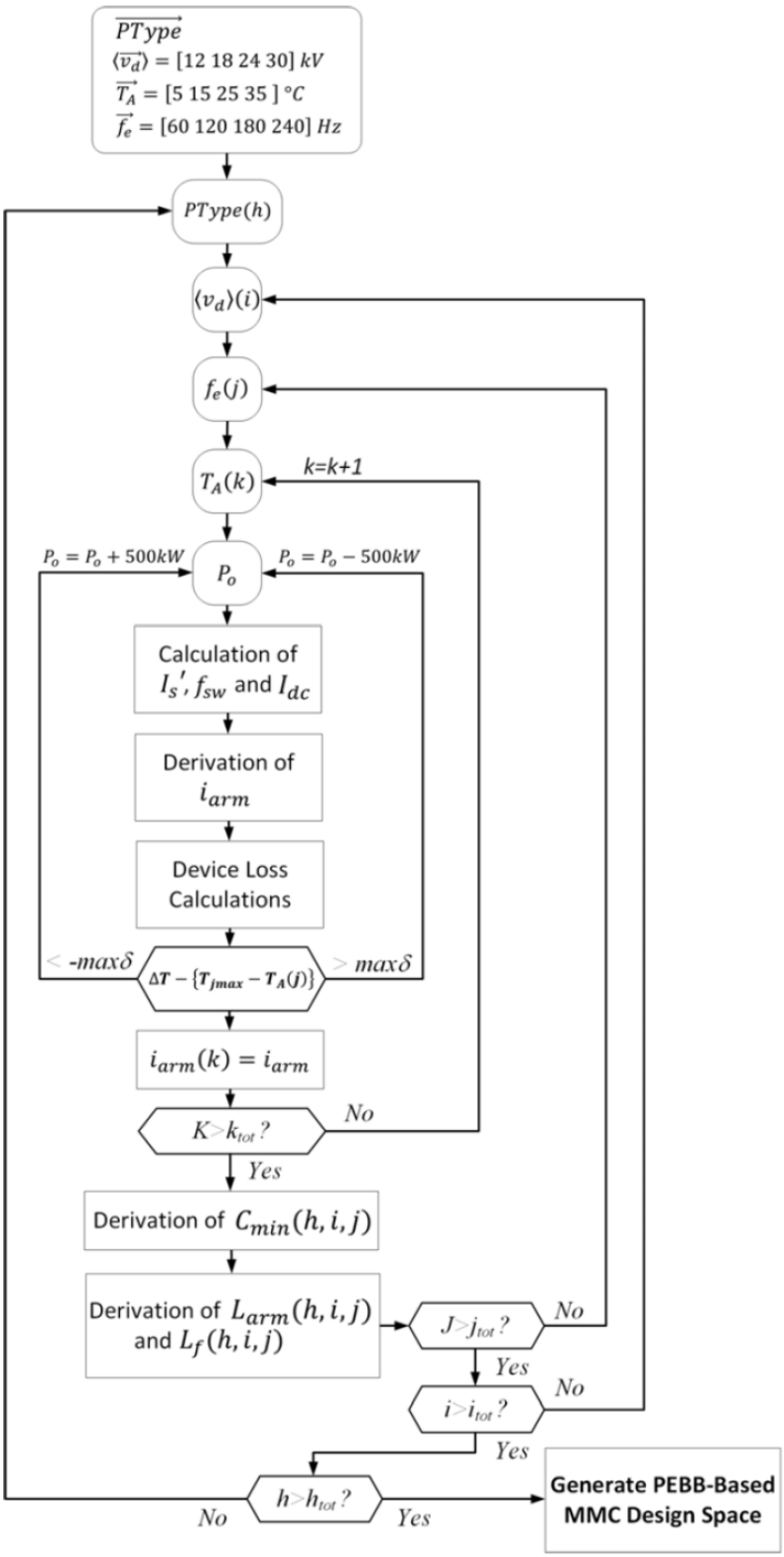

Fig. 2.5: Virtual prototyping process - step 1 [18]

The calculated values become design constraints for the optimal LRU design process and is input into the second step of the VPP along with the LRU design space variables and constraints. The second step of the VPP optimizes the LRU for each design point using a genetic algorithm. The optimized design's physical characteristics and attributes are then input into the third step of the VPP, where the LRUs are arranged into drawers which include system level dimensional allocations for things such as dielectric stand-off, thermal management, frame structure, cabling, etc. The drawers are then arranged into compartments, which are then arranged into bays, with system level dimensional allocations included at each level of arrangement. The result of the third step of the VPP is an optimized bay building block, which is then used to generate a range of module designs over the design space as shown below in Figure 2.6

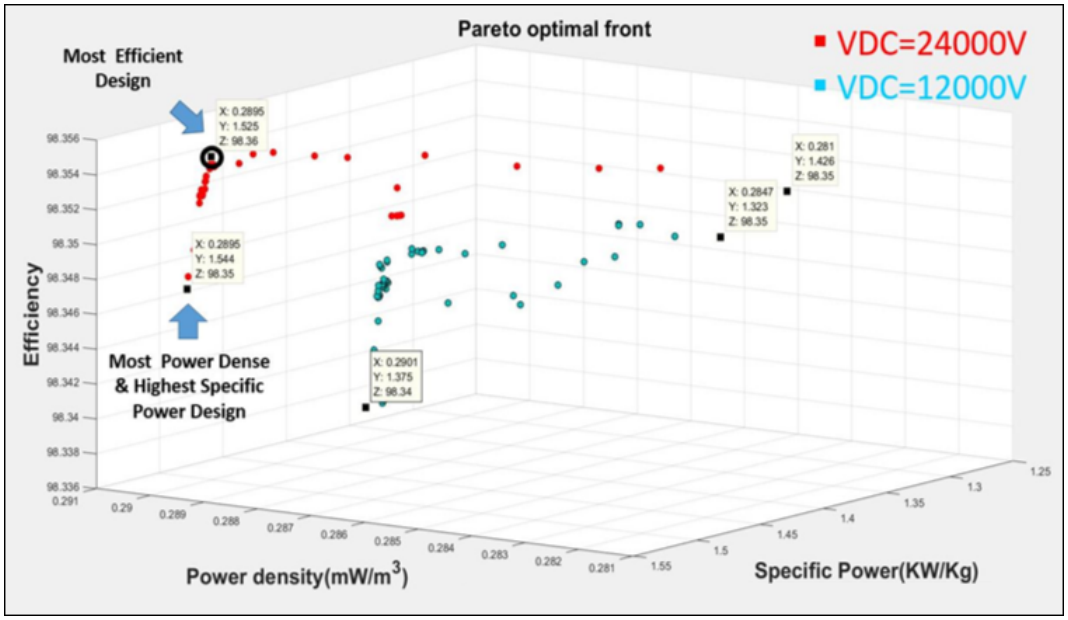

Fig. 2.6: Pareto optimal front [18]

The Genetic Algorithm (GA) embedded within the VPP uses the principles of biological genetics as a computational algorithm for optimization in order to locate a solution, or set of solutions. The use of GAs enables the inclusion of a wider design space through a gene pool $\boldsymbol{\Theta}$, which contains parameters associated with the optimal design of the LRU. The notable differences between traditional optimization algorithms and GAs can be summarized in four

ways. First, GAs operate on an encoding of the argument to the function being optimized rather than the argument of the function being optimized itself. Second, traditional optimization algorithms iterate to improve an estimate for an optimizer, whereas GAs iterate to improve a large number of different estimates of the optimizer. This collection of estimates is known as a *population* and when used, improves the chances of finding a global optimum. Third, GA operations are solely based on the values of the objective function and does not use gradients and Hessians; a useful property for dealing with discontinuous functions and discrete or mixed, i.e., discrete and continuous, search spaces. Lastly, GA operations are based on probabilistic computations rather than deterministic [19].

The GA optimization process used within the VPP can be summarized as consisting of an initialization stage, manipulation of population stage, and a stopping criteria stage. The first generation is created in the Initialization stage. In this stage, a design space is formed by constants and a range of values presented by each *gene*, i.e., each design factor. The LRU models are created through random selections of gene values until an initial population is established. Once an initial population is established, each *member* of the population is evaluated through constraints and assigned a relative fitness value according to success in maximizing or minimizing objectives. This is accomplished through the use of the less-than-or-equal-to and greater-than-or-equal-to functions, defined as

$$\mathrm{lte}(x, x_{mx}) = \begin{cases} 1, & x \leq x_{mx} \\ (1 + x - x_{mx})^{-1}, & x > x_{mx} \end{cases} \tag{2.1}$$

$$\mathrm{gte}(x, x_{mx}) = \begin{cases} 1, & x \geq x_{mx} \\ (1 + x_{mx} - x)^{-1}, & x < x_{mx} \end{cases} \tag{2.2}$$

where x and x_{mx} are the metrics associated with a particular member and a given constraint, respectively.

In the manipulation of population stage, *diversity control* is implemented through the scaling of fitness values in order to prepare the population for selection and prevent the

immediate convergence of designs around any local extrema. Members of the population are then randomly selected to form a *mating pool*, with members possessing high scaled fitness values more likely to be selected. Selected members then enter the *mating* process, which is comprised of chromosome *crossover, segregation, and mutation*, resulting in the generation of *offspring* designs, which while similar to the parent design, have slight genetic variations. During this stage, members of the population are also randomly selected to be removed, with members possessing low fitness values more likely to be removed. This process is known as *death* and serves as a mechanism which holds the size of the population constant.

Once the population has been manipulated, a new generation of the population is established and each member is then evaluated again. This process repeats until a stopping criterion is met and the process enters the stopping criteria stage. The stopping criteria for this particular GA is a specified maximum number of generations. Once satisfied, the remaining population forms the *performance space*, which within the context of [17], contains the set of LRU configurations that have been optimized to the specified objectives. This set of LRU configurations is known as the Pareto front and can be used to describe the trade-offs between competing optimization objectives.

2.4 Scientific Contributions

The VPP implemented by Cuzner *et al* is built off the work done by [20] and distinguishes itself in two significant ways. The first is the incorporation of high frequency behavioral models into the VPP which introduces additional limitations on the design space and various dimensional quantities. The second is the incorporation of spatial and weight allocations associated with insulation, structural interfaces, and cabling between building blocks. This thesis aims to develop the mathematical model for the PEBB LRU while capturing the radiated high frequency effects of WBG devices. The model will inform the VPP through physics-based equations, which can be coded into computational software, and will result in additional constraints derived from the high frequency effects.

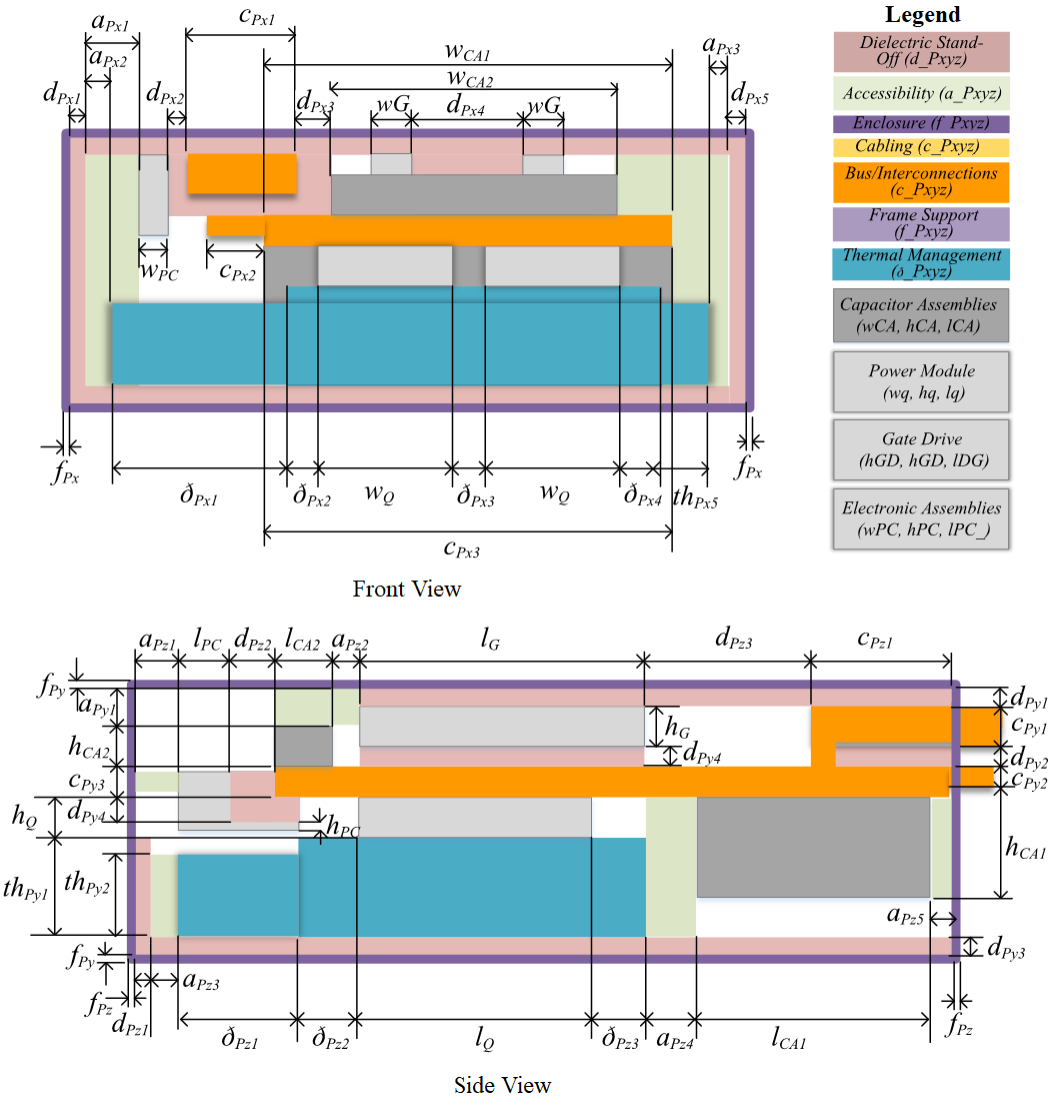

Fig. 2.7: PEBB assembly layout within enclosure

Furthermore, the constraints on the layout of the PEBB assembly derived from this thesis will directly contribute to the 10kV, 240A [21] and 1.7kV, 400A SiC dual modules [22] based PEBB presently being developed at Virginia Tech and will be instrumental in developing the GA within a VPP for the PEBB LRU. To elaborate, a PEBB LRU is laid out with spatial allocations as shown above in Figure 2.7. The PEBB LRU is comprised of a PEBB assembly, which consists of a bus bar, interconnections, a thermal management system, a power module, a gate drive, electronic assemblies and capacitor assemblies, enclosed within metal cavity with space allocations for dielectric material and accessibility.

The shielded enclosure, which encloses the PEBB assembly, is held at ground potential and imposes voltage stand-off requirements on the components internal to the PEBB assembly. In practice, these requirements are satisfied by increasing the distances between components, leading to larger volumes and subsequently, decreased power density. Furthermore, cases have been observed in practice where the PEBB enclosure acts as a resonant cavity, amplifying radiated noise internal to the PEBB and leading to self-compatibility issues. The high frequency model, formulated in the following chapter, is centered around the characterization of the PEBB LRU's inherent cavity modes with the objective of eliminating any resonances and will contribute to the metamodeling approach, the development of a VPP for the PEBB LRU, and provide high frequency constraints on the layout of the PEBB assembly.

Chapter 3

Electromagnetic Theory and Formulation of High Frequency Model

---

The PEBB LRU of Figure 2.7 presents a significant challenge in terms of near field analysis. The in-homogeneity and geometry formed by all of the components necessitates the use of electromagnetic modeling software. Performing such an analysis is not only time consuming and computationally expensive, but also cannot feasibly be integrated into the VPP. Given the objective of developing models which incorporate high frequency effects and the fact that the PEBB assembly is currently under development, it will be assumed that the layout of the internal components which make up the PEBB assembly is variable.

```
PEBB 6000 Dimensions [Empty Cavity]
   0.56 m
   0.80 m
   1.24 m
Resonant Modes Found:
   [n = 0, m = 1, p = 1] at f = 2.236680e+08
   [n = 1, m = 0, p = 1] at f = 2.924399e+08
   [n = 1, m = 1, p = 0] at f = 3.258797e+08
   [n = 1, m = 1, p = 1] at f = 3.476680e+08
   [n = 0, m = 1, p = 2] at f = 3.066816e+08
```

Fig. 3.1: Results of initial calculation of resonant modes

As a first step, the existence of resonant modes were confirmed by assuming an empty air filled cavity with dimensions $\ell = 1.25$ m, $w = 0.8$ m, and $h = 0.565$ m. A simple calculation in MATLAB reveals the existence of modes located within the frequency range of the switching harmonics as summarized by Figure 3.1.

Next, the length, width, and height of the cavity are varied, simulating the existence of a rectangular slab of a Perfect Electrical Conductor (PEC) spanning the plane formed by the cavity's length and width. This step is performed in order to confirm the presence of resonant modes given constraints on length, width, and height used in current layout strategies and assumes that the PEBB assembly is laid out as shown below in Figure 3.2.

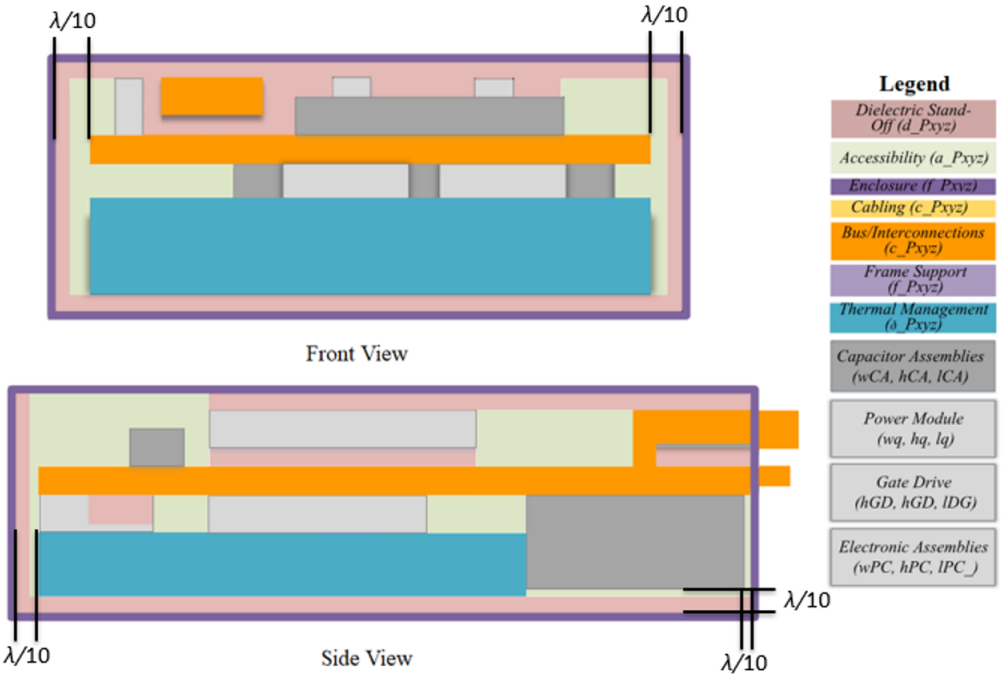

Fig. 3.2: Assumed PEBB assembly layout within enclosure

The layout assumes that the sum of the distances of the dielectric stand-off and accessibility between the enclosure wall and the components are roughly $\lambda/10$. This assumption allows the analysis to neglect any minor cavities formed by the components within the enclosure. Additionally, since a majority of the components below the bus bar are conductors, everything below the uppermost conducting plane of the bus bar can be treated as PEC. These assumptions eliminates the need for any cavity perturbation theories and simplifies

the analysis to a level which can feasibly be incorporated into the VPP. Beginning with the derivation of the Helmholtz equation, this chapter will develop a mathematical model which can be used to obtain the frequency dependent cavity modes and their associated fields and surface current distributions.

3.1 Derivation of the Helmholtz Equations

In the Temporal Fourier Transform domain, Faraday's law (3.1) and Ampére's law (3.2), in Maxwell-Bofi form, are

$$\nabla \times \mathbf{E}(\mathbf{r}) = -i\omega\mu\mathbf{H}(\mathbf{r}) - \mathbf{J}_m(\mathbf{r}) \tag{3.1}$$

$$\nabla \times \mathbf{H}(\mathbf{r}) = i\omega\varepsilon\mathbf{E}(\mathbf{r}) + \mathbf{J}_e(\mathbf{r}). \tag{3.2}$$

For homogeneous media, Maxwell's equations tell us

$$\nabla \cdot \mathbf{H} = 0. \tag{3.3}$$

Since any divergenceless vector is the curl of another vector, we conclude that the relationship between the magnetic field intensity $\mathbf{H}$ and the magnetic vector potential $\mathbf{A}$ to be

$$\mathbf{H} = \nabla \times \mathbf{A}. \tag{3.4}$$

In the absence of magnetic sources, substituting equation 3.4 into equation 3.1 yields

$$\nabla \times (\mathbf{E} + i\omega\mu\mathbf{A}) = 0. \tag{3.5}$$

The vector identity,

$$\nabla \times (\nabla\phi) = 0, \tag{3.6}$$

states that a vector whose curl is zero, is the gradient of a scalar. Thus, we obtain

$$\mathbf{E} + i\omega\mu\mathbf{A} = -\nabla\phi_e, \tag{3.7}$$

where ϕ_e is the electric scalar potential. Substituting equations 3.4 and 3.7 into Ampére's law yields

$$\nabla \times \nabla \times \mathbf{A} = \omega^2\mu\varepsilon\mathbf{A} - i\omega\varepsilon\nabla\phi_e + \mathbf{J}_e, \tag{3.8}$$

which, by the vector identity

$$\nabla \times \nabla \times \mathbf{A} = \nabla(\nabla \cdot \mathbf{A}) - \nabla^2\mathbf{A}, \tag{3.9}$$

can be expressed as

$$\nabla(\nabla \cdot \mathbf{A}) - \nabla^2\mathbf{A} - k^2\mathbf{A} = \mathbf{J}_e - i\omega\varepsilon\nabla\phi_e, \tag{3.10}$$

where $k \equiv \omega\sqrt{\mu\varepsilon}$. The Helmholtz theorem states that a vector field is determined by specifying its curl and divergence. The curl of $\mathbf{A}$ has already been specified by equation 3.4, thus by specifying the divergence of $\mathbf{A}$ as

$$\nabla \cdot \mathbf{A} = -i\omega\varepsilon\phi_e, \tag{3.11}$$

we obtain the Helmholtz equation for the magnetic vector potential,

$$\left(\nabla^2 + k^2\right)\mathbf{A} = -\mathbf{J}_e. \tag{3.12}$$

A dual equation to equation 3.12 can be obtained in a manner similar to that of the above. In the absence of electric sources, since Maxwell's equations tell us that $\nabla \cdot \mathbf{E} = 0$, we

specify the curl of the electric vector potential $\mathbf{F}$ as

$$\mathbf{E} = -\nabla \times \mathbf{F} \tag{3.13}$$

and substitute this into Ampére's law to obtain

$$\nabla \times (\mathbf{H} + i\omega\varepsilon\mathbf{F}) = 0. \tag{3.14}$$

Applying the vector identity outlined in equation 3.7 to equation 3.14 results in

$$\mathbf{H} + i\omega\varepsilon\mathbf{F} = -\nabla\phi_m, \tag{3.15}$$

where ϕ_m is magnetic scalar potential and is the dual to the electric scalar potential ϕ_e. Faraday's law then becomes

$$-\nabla \times \nabla \times \mathbf{F} = -\omega^2\mu\varepsilon\mathbf{F} + i\omega\mu\nabla\phi_m - \mathbf{J}_m, \tag{3.16}$$

which, upon applying the vector identity outlined by equation 3.9 and simplifying, becomes

$$-\nabla(\nabla \cdot \mathbf{F}) + \nabla^2\mathbf{F} + k^2\mathbf{F} = i\omega\mu\nabla\phi_m - \mathbf{J}_m. \tag{3.17}$$

Again, we are free to choose the divergence of $\mathbf{F}$. Thus, by specifying the divergence of $\mathbf{F}$ as

$$\nabla \cdot \mathbf{F} = -i\omega\mu\phi_m, \tag{3.18}$$

we obtain the Helmholtz equation for the electric vector potential.

$$\left(\nabla^2 + k^2\right)\mathbf{F} = -\mathbf{J}_m \tag{3.19}$$

3.2 Codable Formulation of Modal Solutions

When considering multi-objective optimization, it is desirable to have degrees of freedom when analyzing a particular component or sub-system. In this particular case, we seek to find the TE and TM modes of a rectangular cavity for a given set of parameters. The geometric symmetry of a rectangular cavity makes choosing a coordinate which the fields are TE or TM to arbitrary. For this reason, a general method of obtaining the modal solutions will be implemented in order to provide codability to the choice of coordinate.

An advantage of choosing to express the fields in terms of potentials, rather than the fields themselves, is that it allows us to fully exploit the dual nature of the field equations. Furthermore, since the field equations are linear, we can consider the total field to be a superposition of the field due to only electric and only magnetic sources. Thus, in a homogeneous source-free region the total fields can be expressed as

$$\mathbf{E} = \mathbf{E}^m + \mathbf{E}^e \tag{3.20}$$

$$\mathbf{H} = \mathbf{H}^m + \mathbf{H}^e \tag{3.21}$$

where the superscripts m, and e denote the components of the total field due to solely magnetic and electric sources respectively, or expressed in terms of the vector potentials,

$$\mathbf{E} = -\nabla \times \mathbf{F} + \frac{1}{i\omega\varepsilon}\nabla \times \nabla \times \mathbf{A} \tag{3.22}$$

$$\mathbf{H} = \nabla \times \mathbf{A} + \frac{1}{i\omega\mu}\nabla \times \nabla \times \mathbf{F}. \tag{3.23}$$

In the absence of sources, the general equations for the vector potentials derived previously become

$$\nabla \times \nabla \times \mathbf{A} - \omega^2\mu\varepsilon\mathbf{A} = -i\omega\varepsilon\nabla\phi_e \tag{3.24}$$

$$\nabla \times \nabla \times \mathbf{F} - \omega^2\mu\varepsilon\mathbf{F} = -i\omega\mu\nabla\phi_m. \tag{3.25}$$

Then, noting that $\nabla \cdot \mathbf{A} = -i\omega\varepsilon\phi_e$ and $\nabla \cdot \mathbf{F} = -i\omega\mu\phi_m$, we can express $\mathbf{E}$ in a more convenient form by re-arranging equation 3.24

$$\begin{aligned}\nabla \times \nabla \times \mathbf{A} &= -i\omega\varepsilon\nabla\phi_e + \omega^2\mu\varepsilon\mathbf{A} \\ &= \nabla(\nabla \cdot \mathbf{A}) + \omega^2\mu\varepsilon\mathbf{A}\end{aligned}$$

and substituting the result into 3.22 to obtain

$$\begin{aligned}\mathbf{E} &= -\nabla \times \mathbf{F} + \frac{1}{i\omega\varepsilon}\big(\omega^2\mu\varepsilon\mathbf{A} + \nabla(\nabla \cdot \mathbf{A})\big) \\ &= -\nabla \times \mathbf{F} - i\omega\mu\mathbf{A} + \frac{1}{i\omega\varepsilon}\nabla(\nabla \cdot \mathbf{A}).\end{aligned} \tag{3.26}$$

Repeating this for $\mathbf{H}$, the general expressions for the fields become

$$\mathbf{E} = -\nabla \times \mathbf{F} - i\omega\mu\mathbf{A} + \frac{1}{i\omega\varepsilon}\nabla(\nabla \cdot \mathbf{A}) \tag{3.27}$$

$$\mathbf{H} = \nabla \times \mathbf{A} - i\omega\varepsilon\mathbf{F} + \frac{1}{i\omega\mu}\nabla(\nabla \cdot \mathbf{F}). \tag{3.28}$$

Additionally, equations 3.24 and 3.25 reduce to

$$\big(\nabla^2 + k^2\big)\mathbf{A} = 0 \tag{3.29}$$

$$\big(\nabla^2 + k^2\big)\mathbf{F} = 0 \tag{3.30}$$

with the Cartesian components of the magnetic and electric vector potentials also satisfying the scalar Helmholtz equation,

$$\nabla^2\psi + k^2\psi = 0. \tag{3.31}$$

In general, we can write

$$\mathbf{A} = \sum_{i=x,y,z} \psi_i^{(a)}\,\hat{\mathbf{u}}_i \qquad \mathbf{F} = \sum_{i=x,y,z} \psi_i^{(f)}\,\hat{\mathbf{u}}_i \tag{3.32}$$

where ψ_i, also known as the wave function, is a scalar component of the vector potentials guided along the $\hat{\mathbf{u}}_i$ direction. The superscripts a and f are used to distinguish between the wave functions which correspond to $\mathbf{A}$ and $\mathbf{F}$ respectively.

With this formulation, we are able to obtain the fields which are TM or TE to any direction as long as suitable wave functions are known. For example, if we wish to obtain the scalar field components of a field TM to $\hat{\mathbf{x}}$, we choose $\mathbf{F} = 0$ and select

$$\mathbf{A} = \psi_x^{(a)}(\mathbf{r})\,\hat{\mathbf{x}}\,. \tag{3.33}$$

Plugging this in to the field expressions yields

$$\begin{aligned}
\mathbf{E} &= -i\omega\mu\psi_x^{(a)}\,\hat{\mathbf{x}} + \frac{1}{i\omega\varepsilon}\nabla(\nabla\cdot\psi_x^{(a)}\,\hat{\mathbf{x}}) \\
&= -i\omega\mu\psi_x^{(a)}\,\hat{\mathbf{x}} + \frac{1}{i\omega\varepsilon}\left(\frac{\partial^2\psi_x^{(a)}}{\partial x^2}\hat{\mathbf{x}} + \frac{\partial^2\psi_x^{(a)}}{\partial y\partial x}\hat{\mathbf{y}} + \frac{\partial^2\psi_x^{(a)}}{\partial z\partial x}\hat{\mathbf{z}}\right) \\
&= \frac{1}{i\omega\varepsilon}\left(\frac{\partial^2\psi_x^{(a)}}{\partial x^2} + k^2\psi_x^{(a)}\right)\hat{\mathbf{x}} + \frac{1}{i\omega\varepsilon}\frac{\partial^2\psi_x^{(a)}}{\partial y\partial x}\hat{\mathbf{y}} + \frac{1}{i\omega\varepsilon}\frac{\partial^2\psi_x^{(a)}}{\partial z\partial x}\hat{\mathbf{z}} \qquad (3.34)\\
\mathbf{H} &= \nabla\times\psi_x^{(a)}\,\hat{\mathbf{x}} \\
&= \frac{\partial\psi_x^{(a)}}{\partial z}\hat{\mathbf{y}} - \frac{\partial\psi_x^{(a)}}{\partial y}\hat{\mathbf{z}} \qquad (3.35)\\
& \qquad (3.36)
\end{aligned}$$

with the field components

$$\begin{aligned}
E_x &= \frac{1}{i\omega\varepsilon}\left(\frac{\partial^2\psi_x^{(a)}}{\partial x^2} + k^2\psi_x^{(a)}\right) & H_x &= 0 \\
E_y &= \frac{1}{i\omega\varepsilon}\frac{\partial^2\psi_x^{(a)}}{\partial y\partial x} & H_y &= \frac{\partial\psi_x^{(a)}}{\partial z} \\
E_z &= \frac{1}{i\omega\varepsilon}\frac{\partial^2\psi_x^{(a)}}{\partial z\partial x} & H_z &= -\frac{\partial\psi_x^{(a)}}{\partial y}.
\end{aligned}$$

This can be accomplished since modes which are TM to a specified direction, for example, x, are expressible in terms of $\mathbf{A}$ having only a $x-$component and modes which are TE to

x can be expressed in terms of $\mathbf{F}$ having only a $x-$component. Thus, following a similar procedure to that performed above, for $\mathbf{A} = 0$ and

$$\mathbf{F} = \psi_x^{(a)}(\mathbf{r})\,\hat{\mathbf{x}}\,, \tag{3.37}$$

the fields are

$$\begin{aligned}
\mathbf{E} &= -\nabla \times \psi_x^{(f)}\,\hat{\mathbf{x}} \\
&= -\frac{\partial \psi_x^{(f)}}{\partial z}\hat{\mathbf{y}} + \frac{\partial \psi_x^{(f)}}{\partial y}\hat{\mathbf{z}} \qquad (3.38)\\
\mathbf{H} &= -i\omega\varepsilon\psi_x^{(f)}\,\hat{\mathbf{x}} + \frac{1}{i\omega\mu}\nabla(\nabla\cdot\psi_x^{(f)}\,\hat{\mathbf{x}}\,) \\
&= -i\omega\varepsilon\psi_x^{(f)}\,\hat{\mathbf{x}} + \frac{1}{i\omega\mu}\left(\frac{\partial^2\psi_x^{(f)}}{\partial x^2}\hat{\mathbf{x}} + \frac{\partial^2\psi_x^{(f)}}{\partial y\partial x}\hat{\mathbf{y}} + \frac{\partial^2\psi_x^{(f)}}{\partial z\partial x}\hat{\mathbf{z}}\right) \\
&= \frac{1}{i\omega\mu}\left(\frac{\partial^2\psi_x^{(f)}}{\partial x^2} + k^2\psi_x^{(f)}\right)\hat{\mathbf{x}} + \frac{1}{i\omega\mu}\frac{\partial^2\psi_x^{(f)}}{\partial y\partial x}\hat{\mathbf{y}} + \frac{1}{i\omega\mu}\frac{\partial^2\psi_x^{(f)}}{\partial z\partial x}\hat{\mathbf{z}} \qquad (3.39)
\end{aligned}$$

with the field components

$$\begin{aligned}
E_x &= 0 & H_x &= \frac{1}{i\omega\mu}\left(\frac{\partial^2\psi_x^{(f)}}{\partial x^2} + k^2\psi_x^{(f)}\right) \\
E_y &= -\frac{\partial\psi_x^{(f)}}{\partial z} & H_y &= \frac{1}{i\omega\mu}\frac{\partial^2\psi_x^{(f)}}{\partial y\partial x} \\
E_z &= \frac{\partial\psi_x^{(f)}}{\partial y} & H_z &= \frac{1}{i\omega\mu}\frac{\partial^2\psi_x^{(f)}}{\partial z\partial x}.
\end{aligned}$$

Thus leaving only the need to find suitable wave functions.

3.3 Derivation of TE and TM modes

The field equations, expressed in terms of the wave functions, are

$$\mathbf{E} = -\nabla\times\left(\psi_i^{(f)}\,\hat{\mathbf{u}}_i\right) - i\omega\mu\left(\psi_i^{(a)}\,\hat{\mathbf{u}}_i\right) + \frac{1}{i\omega\varepsilon}\nabla\left(\nabla\cdot\left(\psi_i^{(a)}\,\hat{\mathbf{u}}_i\right)\right) \tag{3.40}$$

$$\mathbf{H} = \nabla\times\left(\psi_i^{(a)}\,\hat{\mathbf{u}}_i\right) - i\omega\varepsilon\left(\psi_i^{(f)}\,\hat{\mathbf{u}}_i\right) + \frac{1}{i\omega\mu}\nabla\left(\nabla\cdot\left(\psi_i^{(f)}\,\hat{\mathbf{u}}_i\right)\right). \tag{3.41}$$

With parameterizability in mind, we then seek to construct $\mathbf{A}$ and $\mathbf{F}$ in terms of suitable wave functions.

3.3.1 Wave Functions

To obtain suitable wave functions associated with $\mathbf{A}$ and $\mathbf{F}$, we begin with the vector Helmholtz equation

$$\nabla^2\mathbf{\Psi} + k^2\mathbf{\Psi} = \mathbf{0}, \tag{3.42}$$

where $\mathbf{\Psi}$ represents either $\mathbf{A}$ or $\mathbf{F}$. Expanding and taking a dot product with respect to each component yields three scalar components,

$$\left(\nabla^2 + k^2\right)\psi_x^{a/f}(\mathbf{r}) = 0 \tag{3.43}$$

$$\left(\nabla^2 + k^2\right)\psi_y^{a/f}(\mathbf{r}) = 0 \tag{3.44}$$

$$\left(\nabla^2 + k^2\right)\psi_z^{a/f}(\mathbf{r}) = 0, \tag{3.45}$$

each of which satisfies the scalar Helmholtz equation. The superscript a/f in equations 3.43-3.45 is used here to denote the wave functions associated with both $\mathbf{A}$ and $\mathbf{F}$. Each of these equations is then solved by employing separation of variables, which seeks to obtain solutions which are in the form of

$$\psi_i^{a/f}(\mathbf{r}) = \psi_i^{a/f}(x)\psi_i^{a/f}(y)\psi_i^{a/f}(z) \tag{3.46}$$

where $i = \{x, y, z\}$. Substituting equation 3.46 into the Helmholtz equation

$$\left(\nabla^2 + k^2\right)\psi_i^{a/f}(\mathbf{r}) = 0$$

$$\left(\frac{\partial^2}{\partial x^2} + \frac{\partial^2}{\partial y^2} + \frac{\partial^2}{\partial z^2} + k^2\right)\psi_i^{a/f}(x)\psi_i^{a/f}(y)\psi_i^{a/f}(z) = 0,$$

operating on the wave function with the partial derivatives and multiplying though with $(\psi_i^{a/f}(x)\psi_i^{a/f}(y)\psi_i^{a/f}(z))^{-1}$ yields

$$\frac{1}{\psi_i^{a/f}(x)}\frac{\partial^2\psi_i^{a/f}(x)}{\partial x^2}+\frac{1}{\psi_i^{a/f}(y)}\frac{\partial^2\psi_i^{a/f}(y)}{\partial y^2}+\frac{1}{\psi_i^{a/f}(z)}\frac{\partial^2\psi_i^{a/f}(z)}{\partial z^2}+k^2=0. \tag{3.47}$$

We then define separation constants k_x, k_y, and k_z by letting

$$\frac{1}{\psi_i^{a/f}(x)}\frac{\partial^2\psi_i^{a/f}(x)}{\partial x^2}=-k_x^2 \qquad \frac{1}{\psi_i^{a/f}(y)}\frac{\partial^2\psi_i^{a/f}(y)}{\partial y^2}=-k_y^2 \qquad \frac{1}{\psi_i^{a/f}(z)}\frac{\partial^2\psi_i^{a/f}(z)}{\partial z^2}=-k_z^2 \tag{3.48}$$

such that the separation constants satisfy

$$k_x^2+k_y^2+k_z^2=k^2. \tag{3.49}$$

Thus separating equation 3.47 into three separate equations, leading to

$$\frac{\partial^2\psi_i^{a/f}(x)}{\partial x^2}+k_x^2\psi_i^{a/f}(x)=0 \tag{3.50}$$

$$\frac{\partial^2\psi_i^{a/f}(y)}{\partial y^2}+k_y^2\psi_i^{a/f}(y)=0 \tag{3.51}$$

$$\frac{\partial^2\psi_i^{a/f}(z)}{\partial z^2}+k_z^2\psi_i^{a/f}(z)=0. \tag{3.52}$$

The equations have the characteristic equation

$$\lambda_i^2+k_j^2=0, \tag{3.53}$$

where $i = \{x, y, z\}$ and $j = \{x, y, z\}$ with eigenvalues $\lambda_{i1,i2} = \pm ik_j$ which leads to the eigenfunctions

$$\psi_i^{a/f}(x) = A\sin(k_x x) + B\cos(k_x x) \tag{3.54}$$

$$\psi_i^{a/f}(y) = C\sin(k_y y) + D\cos(k_y y) \tag{3.55}$$

$$\psi_i^{a/f}(z) = E\sin(k_z z) + F\cos(k_z z). \tag{3.56}$$

Thus the general solutions are

$$\psi_x^{a/f}(\mathbf{r}) = [A_1\sin(k_x x) + B_1\cos(k_x x)][C_1\sin(k_y y) + D_1\cos(k_y y)][E_1\sin(k_z z) + F_1\cos(k_z z)] \tag{3.57}$$

$$\psi_y^{a/f}(\mathbf{r}) = [A_2\sin(k_x x) + B_2\cos(k_x x)][C_2\sin(k_y y) + D_2\cos(k_y y)][E_2\sin(k_z z) + F_2\cos(k_z z)] \tag{3.58}$$

$$\psi_z^{a/f}(\mathbf{r}) = [A_3\sin(k_x x) + B_3\cos(k_x x)][C_3\sin(k_y y) + D_3\cos(k_y y)][E_3\sin(k_z z) + F_3\cos(k_z z)]. \tag{3.59}$$

3.3.2 Boundary Conditions

For a rectangular cavity, whose height a, width b, and length c is defined by

$$\{x \in \mathbb{R} \,|\, 0 \le x \le a\}$$

$$\{y \in \mathbb{R} \,|\, 0 \le y \le b\,\}$$

$$\{z \in \mathbb{R} \,|\, 0 \le z \le c\,\},$$

we impose that the tangential components of the electric field vanish at the perfectly conducting cavity walls, i.e., $\mathbf{E}^{\|} = \mathbf{0}$. The symmetry of the cavity allows the fields to be expressed as TM or TE to any coordinate. The simplest approach is to exploit the fact that modes which are TM or TE to the i^{th} coordinate is expressible in terms of $\mathbf{A}$ or $\mathbf{F}$, respectively, having only an i^{th} component.

For the modes which are TM to x, $\mathbf{A} = \psi_x^{(a)}(\mathbf{r})\,\hat{\mathbf{x}}$ and $\mathbf{F} = \mathbf{0}$. The field components are

$$\begin{aligned} E_x &= \frac{1}{i\omega\varepsilon}\left(\frac{\partial^2\psi_x^{(a)}}{\partial x^2} + k^2\psi_x^{(a)}\right) & H_x &= 0 \\ E_y &= \frac{1}{i\omega\varepsilon}\frac{\partial^2\psi_x^{(a)}}{\partial y\partial x} & H_y &= \frac{\partial\psi_x^{(a)}}{\partial z} \\ E_z &= \frac{1}{i\omega\varepsilon}\frac{\partial^2\psi_x^{(a)}}{\partial z\partial x} & H_z &= -\frac{\partial\psi_x^{(a)}}{\partial y}. \end{aligned}$$

The boundary conditions at the cavity walls in the $xz-$plane and the $xy-$plane are satisfied when

$$E_x = \frac{1}{i\omega\varepsilon}\left(\frac{\partial^2\psi_x^{(a)}}{\partial x^2} + k^2\psi_x^{(a)}\right) = \frac{k^2 - k_x^2}{i\omega\varepsilon}\,\psi_x^{(a)} = 0. \tag{3.60}$$

Applying this condition at $\mathbf{r} = (x, y, 0)$ and $\mathbf{r} = (x, 0, z)$, we find

$$\begin{aligned} E_x(x,y,0) &= 0 \\ \frac{k^2-k_x^2}{i\omega\varepsilon}[A_1\sin(k_x x) + B_1\cos(k_x x)][C_1\sin(k_y y) + D_1\cos(k_y y)][E_1\sin(0) + F_1\cos(0)] &= 0 \\ F_1[A_1\sin(k_x x) + B_1\cos(k_x x)][C_1\sin(k_y y) + D_1\cos(k_y y)] &= 0 \\ F_1 &= 0 \end{aligned} \tag{3.61}$$

$$\begin{aligned} E_x(x,0,z) &= 0 \\ \frac{k^2-k_x^2}{i\omega\varepsilon}[A_1\sin(k_x x) + B_1\cos(k_x x)][C_1\sin(0) + D_1\cos(0)]E_1\sin(k_z z) &= 0 \\ D_1[A_1\sin(k_x x) + B_1\cos(k_x x)]E_1\sin(k_z z) &= 0 \\ D_1 &= 0. \end{aligned} \tag{3.62}$$

At $\mathbf{r} = (x, y, c)$ and $\mathbf{r} = (x, b, z)$,

$$
\begin{aligned}
E_x(x, y, c) &= 0 \\
\frac{k^2 - k_x^2}{i\omega\varepsilon}[A_1 \sin(k_x x) + B_1 \cos(k_x x)] C_1 \sin(k_y y) E_1 \sin(k_z c) &= 0 \\
E_1 \sin(k_z c) &= 0 \qquad (3.63) \\
E_x(x, b, z) &= 0 \\
\frac{k^2 - k_x^2}{i\omega\varepsilon}[A_1 \sin(k_x x) + B_1 \cos(k_x x)] C_1 \sin(k_y b) E_1 \sin(k_z z) &= 0 \\
C_1 \sin(k_y b) &= 0. \qquad (3.64)
\end{aligned}
$$

To avoid obtaining the trivial solution, we further impose that $C_1, E_1 \neq 0$, thus imposing that the harmonic functions must be zero. Since the sine function is zero when the argument is either zero or integer multiples of π, we find that

$$
\begin{aligned}
k_y b &= m\pi \\
k_y &= \frac{m\pi}{b} \qquad (3.65) \\
k_z c &= p\pi \\
k_z &= \frac{p\pi}{c} \qquad (3.66)
\end{aligned}
$$

where m and p are integers. Then, at the remaining two walls the tangential components of the electric are E_z and E_y, thus, boundary conditions are satisfied when

$$
E_y = \frac{1}{i\omega\varepsilon} \frac{\partial^2 \psi_x^{(a)}}{\partial y \partial x} = 0. \qquad (3.67)
$$

Then, in terms of $\psi_x^{(a)}$, the tangential electric field is

$$\begin{aligned} E_y &= \frac{1}{i\omega\varepsilon}\frac{\partial^2}{\partial y \partial x}[A_1\sin(k_x x) + B_1\cos(k_x x)]C_1\sin(k_y y)E_1\sin(k_z z) \\ &= C_1E_1\frac{k_x}{i\omega\varepsilon}\frac{\partial}{\partial y}[A_1\cos(k_x x) - B_1\sin(k_x x)]\sin(k_y y)\sin(k_z z) \\ &= C_1E_1\frac{k_xk_y}{i\omega\varepsilon}[A_1\cos(k_x x) - B_1\sin(k_x x)]\cos(k_y y)\sin(k_z z). \end{aligned} \tag{3.68}$$

Applying boundary conditions, at $\mathbf{r} = (0, y, z)$ yields

$$\begin{aligned} E_y(0,y,z) &= 0 \\ C_1E_1\frac{k_xk_y}{i\omega\varepsilon}[A_1\cos(0) - B_1\sin(0)]\cos(k_y y)\sin(k_z z) &= 0 \\ A_1C_1E_1\frac{k_xk_y}{i\omega\varepsilon}\cos(k_y y)\sin(k_z z) &= 0 \\ A_1 &= 0. \end{aligned} \tag{3.69}$$

Then, at $\mathbf{r} = (a, y, z)$ we find

$$\begin{aligned} E_y(a,y,z) &= 0 \\ -B_1C_1E_1\frac{k_xk_y}{i\omega\varepsilon}\sin(k_x a)\cos(k_y y)\sin(k_z z) &= 0 \\ B_1\sin(k_x a) &= 0 \end{aligned} \tag{3.70}$$

and impose the condition that $B_1 \neq$, which leads to

$$k_x = \frac{n\pi}{a}. \tag{3.71}$$

Then, letting $A_x \equiv B_1C_1E_1$, we obtain the scalar $x-$component of $\mathbf{A}$

$$\psi_x^{(a)}(\mathbf{r}) = A_x\cos\Big(\frac{n\pi x}{a}\Big)\sin\Big(\frac{m\pi y}{b}\Big)\sin\Big(\frac{p\pi z}{c}\Big). \tag{3.72}$$

For the modes which are TM to y, $\mathbf{A} = \psi_y^{(a)}(\mathbf{r})\,\hat{\mathbf{y}}$, and $\mathbf{F} = \mathbf{0}$, the field components are

$$\begin{aligned} E_x &= \frac{1}{i\omega\varepsilon}\frac{\partial^2\psi_y^{(a)}}{\partial x\partial y} & H_x &= -\frac{\partial\psi_y^{(a)}}{\partial z} \\ E_y &= \frac{1}{i\omega\varepsilon}\left(\frac{\partial^2\psi_y^{(a)}}{\partial y^2} + k^2\psi_y^{(a)}\right) & H_y &= 0 \\ E_z &= \frac{1}{i\omega\varepsilon}\frac{\partial^2\psi_y^{(a)}}{\partial z\partial y} & H_z &= \frac{\partial\psi_y^{(a)}}{\partial x}. \end{aligned}$$

The boundary conditions at four of the six cavity walls are

$$E_y = \frac{1}{i\omega\varepsilon}\left(\frac{\partial^2\psi_y^{(a)}}{\partial y^2} + k^2\psi_y^{(a)}\right) = \frac{k^2 - k_y^2}{i\omega\varepsilon}\psi_y^{(a)} = 0 \tag{3.73}$$

and

$$E_z = \frac{1}{i\omega\varepsilon}\frac{\partial^2\psi_y^{(a)}}{\partial z\partial y} = 0 \tag{3.74}$$

at the remaining two cavity walls. Following a procedure similar to that used to obtain $\psi_x^{(a)}$, applying boundary conditions at $x = 0$ and $z = 0$, leads to $B_2 = F_2 = 0$; and imposing $A_2, E_2 \neq 0$ at $x = a$ and $z = c$ leads to

$$k_x = \frac{n\pi}{a} \qquad k_z = \frac{p\pi}{c}.$$

The tangential field at the remaining cavity walls is given by

$$\begin{aligned} E_z &= A_2E_2\frac{1}{i\omega\varepsilon}\frac{\partial^2}{\partial z\partial y}\sin(k_x x)[C_2\sin(k_y y) + D_2\cos(k_y y)]\sin(k_z z) \\ &= A_2E_2\frac{k_y}{i\omega\varepsilon}\frac{\partial}{\partial z}\sin(k_x x)[C_2\cos(k_y y) - D_2\sin(k_y y)]\sin(k_z z) \\ &= A_2E_2\frac{k_y k_z}{i\omega\varepsilon}\sin(k_x x)[C_2\cos(k_y y) - D_2\sin(k_y y)]\cos(k_z z). \end{aligned} \tag{3.75}$$

Then, applying boundary conditions at $y = 0$ and $y = b$ leads to $C_2 = 0$ and

$$k_y = \frac{m\pi}{b}. \tag{3.76}$$

Thus, the scalar $y-$component of $\mathbf{A}$ is

$$\psi_y^{(a)}(\mathbf{r}) = A_y \sin\Big(\frac{n\pi x}{a}\Big) \cos\Big(\frac{m\pi y}{b}\Big) \sin\Big(\frac{p\pi z}{c}\Big). \tag{3.77}$$

where $A_y \equiv A_2 D_2 E_2$. Lastly, for the modes which are TM to z, $\mathbf{A} = \psi_z^{(a)}(\mathbf{r})\,\hat{\mathbf{z}}$, and $\mathbf{F} = \mathbf{0}$, the field components are

$$\begin{aligned}
E_x &= \frac{1}{i\omega\varepsilon}\frac{\partial^2\psi_z^{(a)}}{\partial x \partial z} & H_x &= \frac{\partial\psi_z^{(a)}}{\partial y} \\
E_y &= \frac{1}{i\omega\varepsilon}\frac{\partial^2\psi_z^{(a)}}{\partial y \partial z} & H_y &= -\frac{\partial\psi_z^{(a)}}{\partial x} \\
E_z &= \frac{1}{i\omega\varepsilon}\left(\frac{\partial^2\psi_z^{(a)}}{\partial z^2} + k^2\psi_z^{(a)}\right) & H_z &= 0.
\end{aligned}$$

The boundary conditions at four of the six cavity walls are

$$E_z = \frac{1}{i\omega\varepsilon}\left(\frac{\partial^2\psi_z^{(a)}}{\partial z^2} + k^2\psi_z^{(a)}\right) = \frac{k^2 - k_z^2}{i\omega\varepsilon}\psi_z^{(a)} = 0 \tag{3.78}$$

and

$$E_x = \frac{1}{i\omega\varepsilon}\frac{\partial^2\psi_z^{(a)}}{\partial x \partial z} = 0 \tag{3.79}$$

at remaining two. Applying boundary conditions at $x = 0$ and $y = 0$, leads to $B_3 = D_3 = 0$; and imposing $A_3, C_3 \neq 0$ at $x = a$ and $y = b$ leads to

$$k_x = \frac{n\pi}{a} \qquad k_y = \frac{m\pi}{b}.$$

The tangential field at the remaining cavity walls is given by

$$\begin{aligned} E_x &= A_3 C_3 \frac{1}{i\omega\varepsilon} \frac{\partial^2}{\partial x \partial z} \sin(k_x x) \sin(k_y y)[E_3 \sin(k_z z) + F_3 \cos(k_z z)] \\ &= A_3 C_3 \frac{k_z}{i\omega\varepsilon} \frac{\partial}{\partial x} \sin(k_x x) \sin(k_y y)[E_3 \cos(k_z z) - F_3 \sin(k_z z)] \\ &= A_3 C_3 \frac{k_z k_x}{i\omega\varepsilon} \cos(k_x x) \sin(k_y y)[E_3 \cos(k_z z) - F_3 \sin(k_z z)]. \end{aligned} \tag{3.80}$$

Then, applying boundary conditions at $z = 0$ and $z = c$ leads to $E_3 = 0$ and

$$k_z = \frac{p\pi}{c}. \tag{3.81}$$

Thus, the scalar $z-$component of $\mathbf{A}$ is

$$\psi_z^{(a)}(\mathbf{r}) = A_z \sin\Big(\frac{n\pi x}{a}\Big) \sin\Big(\frac{m\pi y}{b}\Big) \cos\Big(\frac{p\pi z}{c}\Big), \tag{3.82}$$

where $A_z \equiv A_3 C_3 F_3$. Thus, $\mathbf{A}$ is then

$$\mathbf{A}(\mathbf{r}) = \begin{pmatrix} A_x \cos(n_x \pi x/a) \sin(m_x \pi y/b) \sin(p_x \pi z/c) \\ A_y \sin(n_y \pi x/a) \cos(m_y \pi y/b) \sin(p_y \pi z/c) \\ A_z \sin(n_z \pi x/a) \sin(m_z \pi y/b) \cos(p_z \pi z/c) \end{pmatrix}, \tag{3.83}$$

where the subscripts x, y, and z have been used to distinguish between integers of different components with

$$k_{nmp} = \sqrt{\Big(\frac{n_i \pi}{a}\Big)^2 + \Big(\frac{m_i \pi}{b}\Big)^2 + \Big(\frac{p_i \pi}{c}\Big)^2} \tag{3.84}$$

and

$$n_x = 0, 1, 2, ..., \quad m_x = 1, 2, 3, ..., \quad p_x = 1, 2, 3, ... \tag{3.85}$$

$$n_y = 1, 2, 3, ..., \quad m_y = 0, 1, 2, ..., \quad p_y = 1, 2, 3, ... \tag{3.86}$$

$$n_z = 1, 2, 3, ..., \quad m_z = 1, 2, 3, ..., \quad p_z = 0, 1, 2, ... \tag{3.87}$$

Furthermore, with $k = \omega\sqrt{\mu\varepsilon}$, a general expression for the resonant frequency can be obtained for a given mode TM to a specified direction

$$f_{\mathrm{TM}} = \frac{1}{2\sqrt{\mu\varepsilon}}\sqrt{\left(\frac{n_i}{a}\right)^2 + \left(\frac{m_i}{b}\right)^2 + \left(\frac{p_i}{c}\right)^2} \tag{3.88}$$

where $i = \{x, y, z\}$. For the TE modes, the same procedure is followed while using the dual nature of the equations.

For modes which are TE to x, $\mathbf{F} = \psi_x^{(f)}(\mathbf{r})\,\hat{\mathbf{x}}$ and $\mathbf{A} = \mathbf{0}$. The field components are

$$\begin{aligned}
E_x &= 0 & H_x &= \frac{1}{i\omega\mu}\left(\frac{\partial^2\psi_x^{(f)}}{\partial x^2} + k^2\psi_x^{(f)}\right)\\
E_y &= -\frac{\partial\psi_x^{(f)}}{\partial z} & H_y &= \frac{1}{i\omega\mu}\frac{\partial^2\psi_x^{(f)}}{\partial y\partial x}\\
E_z &= \frac{\partial\psi_x^{(f)}}{\partial y} & H_z &= \frac{1}{i\omega\mu}\frac{\partial^2\psi_x^{(f)}}{\partial z\partial x}.
\end{aligned}$$

The boundary conditions at the four cavity walls in the $xy-$plane and the $yz-$plane and the two cavity walls in the $xz-$plane are

$$E_y = -\frac{\partial\psi_x^{(f)}}{\partial z} = 0 \tag{3.89}$$

$$E_z = \frac{\partial\psi_x^{(f)}}{\partial y} = 0 \tag{3.90}$$

respectively. Applying boundary conditions at $z = 0$ and $x = 0$ leads to

$$\begin{aligned}
-\frac{\partial \psi_x^{(f)}(x, y, 0)}{\partial z} &= 0 \\
-k_z[A_1 \sin(k_x x) + B_1 \cos(k_x x)][C_1 \sin(k_y y) + D_1 \cos(k_y y)][E_1 \cos(0) - F_1 \sin(0)] &= 0 \\
-E_1 k_z[A_1 \sin(k_x x) + B_1 \cos(k_x x)][C_1 \sin(k_y y) + D_1 \cos(k_y y)] &= 0 \\
E_1 &= 0
\end{aligned} \tag{3.91}$$

$$\begin{aligned}
-\frac{\partial \psi_x^{(f)}(0, y, z)}{\partial z} &= 0 \\
-k_z[A_1 \sin(0) + B_1 \cos(0)][C_1 \sin(k_y y) + D_1 \cos(k_y y)][-F_1 \sin(k_z z)] &= 0 \\
B_1 k_z[C_1 \sin(k_y y) + D_1 \cos(k_y y)] F_1 \sin(k_z z) &= 0 \\
B_1 &= 0,
\end{aligned} \tag{3.92}$$

and applying boundary conditions at $z = c$ and $x = a$ leads to

$$k_x = \frac{u\pi}{a} \tag{3.93}$$

$$k_y = \frac{w\pi}{c}. \tag{3.94}$$

Applying boundary conditions at $y = 0$ and $y = b$, we find

$$\begin{aligned}
\frac{\partial \psi_x^{(f)}(x, 0, z)}{\partial y} &= 0 \\
k_y A_1 \sin(k_x x)[C_1 \cos(0) - D_1 \sin(0)][-F_1 \sin(k_z z)] &= 0 \\
-C_1 k_y A_1 \sin(k_x x) F_1 \sin(k_z z) &= 0 \\
C_1 &= 0
\end{aligned} \tag{3.95}$$

and

$$k_y = \frac{v\pi}{b}. \tag{3.96}$$

Thus, setting $F_x \equiv A_1 D_1 F_1$, the scalar $x-$component of $\mathbf{F}$ is

$$\psi_x^{(f)}(\mathbf{r}) = F_x \sin\Big(\frac{u\pi x}{a}\Big)\cos\Big(\frac{v\pi y}{b}\Big)\cos\Big(\frac{w\pi z}{c}\Big). \tag{3.97}$$

For modes which are TE to y, $\mathbf{F} = \psi_y^{(f)}(\mathbf{r})\,\hat{\mathbf{y}}$ and $\mathbf{A} = \mathbf{0}$. The field components are

$$\begin{aligned}
E_x &= \frac{\partial \psi_y^{(f)}}{\partial z} \qquad & H_x &= \frac{1}{i\omega\mu}\frac{\partial^2 \psi_y^{(f)}}{\partial x \partial y} \\
E_y &= 0 & H_y &= \frac{1}{i\omega\mu}\left(\frac{\partial^2 \psi_y^{(f)}}{\partial y^2} + k^2 \psi_y^{(f)}\right) \\
E_z &= -\frac{\partial \psi_y^{(f)}}{\partial x} & H_z &= \frac{1}{i\omega\mu}\frac{\partial^2 \psi_y^{(f)}}{\partial z \partial y}.
\end{aligned}$$

The boundary conditions at the four cavity walls in the $xy-$plane and the $xz-$plane and the two cavity walls in the $yz-$plane are

$$E_x = \frac{\partial \psi_y^{(f)}}{\partial z} = 0 \tag{3.98}$$

$$E_z = -\frac{\partial \psi_y^{(f)}}{\partial x} = 0 \tag{3.99}$$

respectively. Noting that

$$\begin{aligned}
E_x(x,y,z) = k_z\Big(&[A_2\sin(k_x x) + B_2\cos(k_x x)] \\
&[C_2\sin(k_y y) + D_2\cos(k_y y)][E_2\cos(k_z z) - F_2\sin(k_z z)]\Big)
\end{aligned} \tag{3.100}$$

$$\begin{aligned}
E_z(x,y,z) = -k_x\Big(&[A_2\cos(k_x x) - B_2\sin(k_x x)] \\
&[C_2\sin(k_y y) + D_2\cos(k_y y)][E_2\sin(k_z z) + F_2\cos(k_z z)]\Big)
\end{aligned} \tag{3.101}$$

and applying boundary conditions leads to $A_2 = D_2 = E_2 = 0$, with

$$k_x = \frac{u\pi}{a} \qquad k_y = \frac{v\pi}{b} \qquad k_z = \frac{w\pi}{c}. \tag{3.102}$$

Thus obtaining the scalar $y-$component of $\mathbf{F}$

$$\psi_x^{(f)}(\mathbf{r}) = F_y \cos\Big(\frac{u\pi x}{a}\Big) \sin\Big(\frac{v\pi y}{b}\Big) \cos\Big(\frac{w\pi z}{c}\Big) \tag{3.103}$$

where $F_y \equiv A_2 D_2 E_2$.

For the modes TE to z, $\mathbf{F} = \psi_z^{(f)}(\mathbf{r})\,\hat{\mathbf{z}}$ and $\mathbf{A} = \mathbf{0}$. The field components are given by

$$\begin{aligned}
E_x &= -\frac{\partial \psi_z^{(f)}}{\partial y} \qquad & H_x &= \frac{1}{i\omega\mu}\frac{\partial^2 \psi_z^{(f)}}{\partial x \partial z} \\
E_y &= \frac{\partial \psi_z^{(f)}}{\partial x} \qquad & H_y &= \frac{1}{i\omega\mu}\frac{\partial^2 \psi_z^{(f)}}{\partial y \partial z} \\
E_z &= 0 \qquad & H_z &= \frac{1}{i\omega\mu}\left(\frac{\partial^2 \psi_z^{(f)}}{\partial z^2} + k^2 \psi_z^{(f)}\right).
\end{aligned}$$

Noting that,

$$\begin{aligned}
E_x(x,y,z) = -k_y\Big(&[A_3 \sin(k_x x) + B_3 \cos(k_x x)] \\
&[C_3 \cos(k_y y) - D_3 \sin(k_y y)][E_3 \sin(k_z z) + F_3 \cos(k_z z)]\Big)
\end{aligned} \tag{3.104}$$

$$\begin{aligned}
E_z(x,y,z) = k_x\Big(&[A_3 \cos(k_x x) - B_3 \sin(k_x x)] \\
&[C_3 \sin(k_y y) + D_3 \cos(k_y y)][E_3 \sin(k_z z) + F_3 \cos(k_z z)]\Big),
\end{aligned} \tag{3.105}$$

and imposing that the tangential components of $\mathbf{E}$ are zero at the cavity walls; we find that at $E_z(0,y,z)$, $A_3 = 0$; at $E_z(x,0,z)$, $D_3 = 0$; and at $E_x(x,y,0)$, $F_3 = 0$. Then, applying boundary conditions at $E_z(a,y,z)$, $E_z(x,b,z)$, and $E_x(x,y,c)$ leads to

$$k_x = \frac{u\pi}{a} \qquad k_y = \frac{v\pi}{b} \qquad k_z = \frac{w\pi}{c}. \tag{3.106}$$

The resulting expression for the scalar $z-$component of $\mathbf{F}$ is

$$\psi_x^{(f)}(\mathbf{r}) = F_z \cos\Big(\frac{u\pi x}{a}\Big) \cos\Big(\frac{v\pi y}{b}\Big) \sin\Big(\frac{w\pi z}{c}\Big). \tag{3.107}$$

Thus, $\mathbf{F}$ is then

$$\mathbf{F}(\mathbf{r}) = \begin{pmatrix} F_x \sin(u_x \pi x/a) \cos(v_x \pi y/b) \cos(w_x \pi z/c) \\ F_y \cos(u_y \pi x/a) \sin(v_y \pi y/b) \cos(w_y \pi z/c) \\ F_z \cos(u_z \pi x/a) \cos(v_z \pi y/b) \sin(w_z \pi z/c) \end{pmatrix}, \tag{3.108}$$

where the subscripts x, y, and z have been once again used to distinguish between integers of different components with

$$k_{uvw} = \sqrt{\left(\frac{u_i \pi}{a}\right)^2 + \left(\frac{v_i \pi}{b}\right)^2 + \left(\frac{w_i \pi}{c}\right)^2}, \tag{3.109}$$

where $i = \{x, y, z\}$ and

$$u_x = 1, 2, 3, ..., \quad v_x = 0, 1, 2, ..., \quad w_x = 0, 1, 2, ..., \quad v_z = w_z = 0 \text{ excepted} \tag{3.110}$$

$$u_y = 0, 1, 2, ..., \quad v_y = 1, 2, 3, ..., \quad w_y = 0, 1, 2, ..., \quad u_z = w_z = 0 \text{ excepted} \tag{3.111}$$

$$u_z = 0, 1, 2, ..., \quad v_z = 0, 1, 2, ..., \quad w_z = 1, 2, 3, ..., \quad u_z = v_z = 0 \text{ excepted.} \tag{3.112}$$

As it was the case with the TM modes, since $k = \omega\sqrt{\mu\varepsilon}$,

$$f_{\text{TE}} = \frac{1}{2\sqrt{\mu\varepsilon}} \sqrt{\left(\frac{u_i}{a}\right)^2 + \left(\frac{v_i}{b}\right)^2 + \left(\frac{w_i}{c}\right)^2}. \tag{3.113}$$

3.4 Electric and Magnetic Field Expressions

As previously mentioned, the fields which are TE or TM to the i^{th} direction, are obtained by substituting the $i^{\text{th}}-$component of equations 3.83 and 3.108 into

$$\mathbf{E} = -\nabla \times \mathbf{F} - i\omega\mu\mathbf{A} + \frac{1}{i\omega\varepsilon}\nabla(\nabla \cdot \mathbf{A}) \tag{3.114}$$

$$\mathbf{H} = \nabla \times \mathbf{A} - i\omega\varepsilon\mathbf{F} + \frac{1}{i\omega\mu}\nabla(\nabla \cdot \mathbf{F}) \tag{3.115}$$

and employing superposition. Having derived every component of $\mathbf{A}$ and $\mathbf{F}$, it is sufficient to consider modes TM and TE to one specified direction. It is conventional in electromagnetic theory to classify modes as TM and TE to z; for the remainder of the this work, the same convention will be followed.

3.4.1 TM^z Fields

For TM^z fields,

$$\mathbf{A} = \sin\Big(\frac{n_z\pi x}{a}\Big)\sin\Big(\frac{m_z\pi y}{b}\Big)\cos\Big(\frac{p_z\pi z}{c}\Big)\,\hat{\mathbf{z}}\,, \quad \mathbf{F} = \mathbf{0}. \tag{3.116}$$

Substituting into equations 3.114-3.115, the electric field is then

$$\begin{aligned}
\mathbf{E} &= -i\omega\mu\sin\Big(\frac{n_z\pi x}{a}\Big)\sin\Big(\frac{m_z\pi y}{b}\Big)\cos\Big(\frac{p_z\pi z}{c}\Big)\hat{\mathbf{z}} \\
&\quad + \frac{1}{i\omega\varepsilon}\nabla\Big(\nabla\cdot\sin\Big(\frac{n_z\pi x}{a}\Big)\sin\Big(\frac{m_z\pi y}{b}\Big)\cos\Big(\frac{p_z\pi z}{c}\Big)\hat{\mathbf{z}}\Big) \\
&= -i\omega\mu\sin\Big(\frac{n_z\pi x}{a}\Big)\sin\Big(\frac{m_z\pi y}{b}\Big)\cos\Big(\frac{p_z\pi z}{c}\Big)\hat{\mathbf{z}} - \frac{p_z\pi}{i\omega\varepsilon c}\nabla\sin\Big(\frac{n_z\pi x}{a}\Big)\sin\Big(\frac{m_z\pi y}{b}\Big)\sin\Big(\frac{p_z\pi z}{c}\Big) \\
&= -\frac{n_z p_z\pi^2}{i\omega\varepsilon ac}\cos\Big(\frac{n_z\pi x}{a}\Big)\sin\Big(\frac{m_z\pi y}{b}\Big)\sin\Big(\frac{p_z\pi z}{c}\Big)\hat{\mathbf{x}} \\
&\quad - \frac{m_z p_z\pi^2}{i\omega\varepsilon bc}\sin\Big(\frac{n_z\pi x}{a}\Big)\cos\Big(\frac{m_z\pi y}{b}\Big)\sin\Big(\frac{p_z\pi z}{c}\Big)\hat{\mathbf{y}} \\
&\quad - \left(\frac{p_z^2\pi^2}{i\omega\varepsilon c^2} + i\omega\mu\right)\sin\Big(\frac{n_z\pi x}{a}\Big)\sin\Big(\frac{m_z\pi y}{b}\Big)\cos\Big(\frac{p_z\pi z}{c}\Big)\hat{\mathbf{z}}\,,
\end{aligned}$$

which simplifies to

$$\mathbf{E} = \frac{i\pi^2}{\omega\varepsilon}\begin{pmatrix} \frac{n_z p_z}{ac}\cos\big(\frac{n_z\pi x}{a}\big)\sin\big(\frac{m_z\pi y}{b}\big)\sin\big(\frac{p_z\pi z}{c}\big) \\ \frac{m_z p_z}{bc}\sin\big(\frac{n_z\pi x}{a}\big)\cos\big(\frac{m_z\pi y}{b}\big)\sin\big(\frac{p_z\pi z}{c}\big) \\ \Big(\frac{p_z^2}{c^2} - \frac{k^2}{\pi^2}\Big)\sin\big(\frac{n_z\pi x}{a}\big)\sin\big(\frac{m_z\pi y}{b}\big)\cos\big(\frac{p_z\pi z}{c}\big) \end{pmatrix}, \tag{3.117}$$

and the magnetic field is

$$\begin{aligned}\mathbf{H} &= \boldsymbol{\nabla} \times \sin\Big(\frac{n_z\pi x}{a}\Big)\sin\Big(\frac{m_z\pi y}{b}\Big)\cos\Big(\frac{p_z\pi z}{c}\Big)\hat{\mathbf{z}} \\ &= \frac{m_z\pi}{b}\sin\Big(\frac{n_z\pi x}{a}\Big)\cos\Big(\frac{m_z\pi y}{b}\Big)\cos\Big(\frac{p_z\pi z}{c}\Big)\hat{\mathbf{x}} - \frac{n_z\pi}{a}\cos\Big(\frac{n_z\pi x}{a}\Big)\sin\Big(\frac{m_z\pi y}{b}\Big)\cos\Big(\frac{p_z\pi z}{c}\Big)\hat{\mathbf{y}}\,.\end{aligned} \tag{3.118}$$

For modes TM to z, $n_z = 1, 2, 3, ...$; $m_z = 1, 2, 3, ...$; and $p_z = 0, 1, 2, ...$ The magnitude of the electric and magnetic fields for the first TM mode, which is the TM_{110} mode, are shown in Figures 3.3 and 3.4 below in order to visualize the fields.

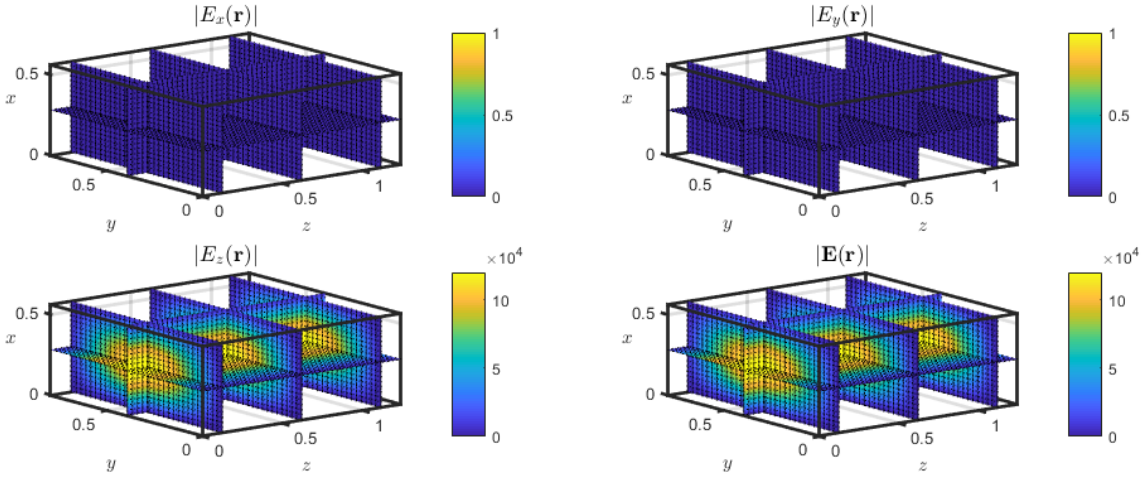

Fig. 3.3: Plot of $|E_x(\mathbf{r})|$, $|E_y(\mathbf{r})|$, $|E_z(\mathbf{r})|$, and $|\mathbf{E}(\mathbf{r})|$ for the TM_{110} mode

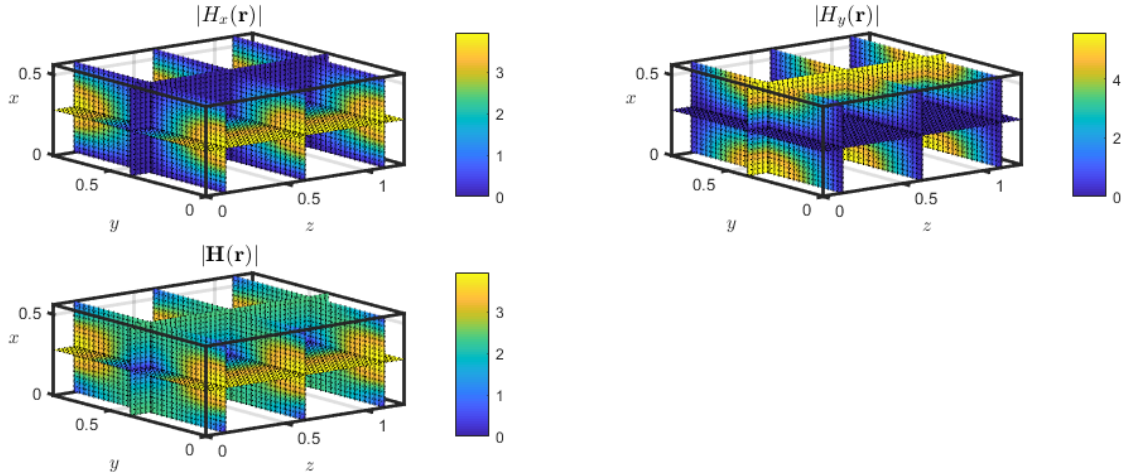

Fig. 3.4: Plot of $|H_x(\mathbf{r})|$, $|H_y(\mathbf{r})|$, and $|\mathbf{H}(\mathbf{r})|$ for the TM_{110} mode

The fields are shown within a rectangular cavity with $c = 0.56$ m, $b = 0.8$ m, and $a = 1.2$ m. Given the assumptions on the layout which were made in the beginning of this chapter, the fields which are plotted are not exactly the same as the fields within the actual enclosure, however, the information can be used as an early approximation to obtain optimal designs and can be later refined within electromagnetic modeling software once a design is selected. The electric field, having only a z-component, is strongest at $(x, y) = (0.26, 0.4)$ for all values of z. The magnetic field has both, a x and y-component and is at a maximum at $(x, y) = (0.26, 0)$ and $(x, y) = (0.26, 0.8)$ for all values of z.

3.4.2 TE^z Fields

For TE^z fields,

$$\mathbf{A} = \mathbf{0}, \quad \mathbf{F} = \cos\Big(\frac{u_z \pi x}{a}\Big) \cos\Big(\frac{v_z \pi y}{b}\Big) \sin\Big(\frac{w_z \pi z}{c}\Big)\, \hat{\mathbf{z}}\,. \tag{3.119}$$

Substituting into equations 3.114-3.115 yields

$$\begin{aligned}\mathbf{E} &= -\boldsymbol{\nabla} \times \cos\Big(\frac{u_z \pi x}{a}\Big) \cos\Big(\frac{v_z \pi y}{b}\Big) \sin\Big(\frac{w_z \pi z}{c}\Big)\hat{\mathbf{z}} \\ &= \frac{v_z \pi}{b} \cos\Big(\frac{u_z \pi x}{a}\Big) \sin\Big(\frac{v_z \pi y}{b}\Big) \sin\Big(\frac{w_z \pi z}{c}\Big)\hat{\mathbf{x}} - \frac{u_z \pi}{a} \sin\Big(\frac{u_z \pi x}{a}\Big) \cos\Big(\frac{v_z \pi y}{b}\Big) \sin\Big(\frac{w_z \pi z}{c}\Big)\hat{\mathbf{y}}\end{aligned} \tag{3.120}$$

and

$$\begin{aligned}
\mathbf{H} &= -i\omega\varepsilon\cos\Big(\frac{u_z\pi x}{a}\Big)\cos\Big(\frac{v_z\pi y}{b}\Big)\sin\Big(\frac{w_z\pi z}{c}\Big)\hat{\mathbf{z}} \\
&\quad + \frac{1}{i\omega\mu}\nabla\Big(\nabla\cdot\cos\Big(\frac{u_z\pi x}{a}\Big)\cos\Big(\frac{v_z\pi y}{b}\Big)\sin\Big(\frac{w_z\pi z}{c}\Big)\hat{\mathbf{z}}\Big) \\
&= -i\omega\varepsilon\cos\Big(\frac{u_z\pi x}{a}\Big)\cos\Big(\frac{v_z\pi y}{b}\Big)\sin\Big(\frac{w_z\pi z}{c}\Big)\hat{\mathbf{z}} \\
&\quad + \frac{w_z\pi}{i\omega\mu c}\nabla\cos\Big(\frac{u_z\pi x}{a}\Big)\cos\Big(\frac{v_z\pi y}{b}\Big)\cos\Big(\frac{w_z\pi z}{c}\Big) \\
&= -\frac{u_z w_z\pi^2}{i\omega\mu ac}\sin\Big(\frac{u_z\pi x}{a}\Big)\cos\Big(\frac{v_z\pi y}{b}\Big)\cos\Big(\frac{w_z\pi z}{c}\Big)\hat{\mathbf{x}} \\
&\quad - \frac{v_z w_z\pi^2}{i\omega\mu bc}\cos\Big(\frac{u_z\pi x}{a}\Big)\sin\Big(\frac{v_z\pi y}{b}\Big)\cos\Big(\frac{w_z\pi z}{c}\Big)\hat{\mathbf{y}} \\
&\quad - \left(\frac{w_z^2\pi^2}{i\omega\mu c^2} + i\omega\varepsilon\right)\cos\Big(\frac{u_z\pi x}{a}\Big)\cos\Big(\frac{v_z\pi y}{b}\Big)\sin\Big(\frac{w_z\pi z}{c}\Big)\hat{\mathbf{z}}
\end{aligned}$$

which simplifies to

$$\mathbf{H} = \frac{i\pi^2}{\omega\mu}\begin{pmatrix} \frac{u_z w_z}{ac}\sin\big(\frac{u_z\pi x}{a}\big)\cos\big(\frac{v_z\pi y}{b}\big)\cos\big(\frac{w_z\pi z}{c}\big) \\ \frac{v_z w_z}{bc}\cos\big(\frac{u_z\pi x}{a}\big)\sin\big(\frac{v_z\pi y}{b}\big)\cos\big(\frac{w_z\pi z}{c}\big) \\ \Big(\frac{w_z^2}{c^2} - \frac{k^2}{\pi^2}\Big)\cos\big(\frac{u_z\pi x}{a}\big)\cos\big(\frac{v_z\pi y}{b}\big)\sin\big(\frac{w_z\pi z}{c}\big) \end{pmatrix} \tag{3.121}$$

For modes TE to z, $u_z = 0, 1, 2, ...$; $v_z = 0, 1, 2, ...$; $w_z = 1, 2, 3, ...$ with $u_z = v_z = 0$ excepted. The magnitudes of the fields and their components for the TE_{011} mode within a cavity of the same dimensions as in Figures 3.3 and 3.4 are shown below.

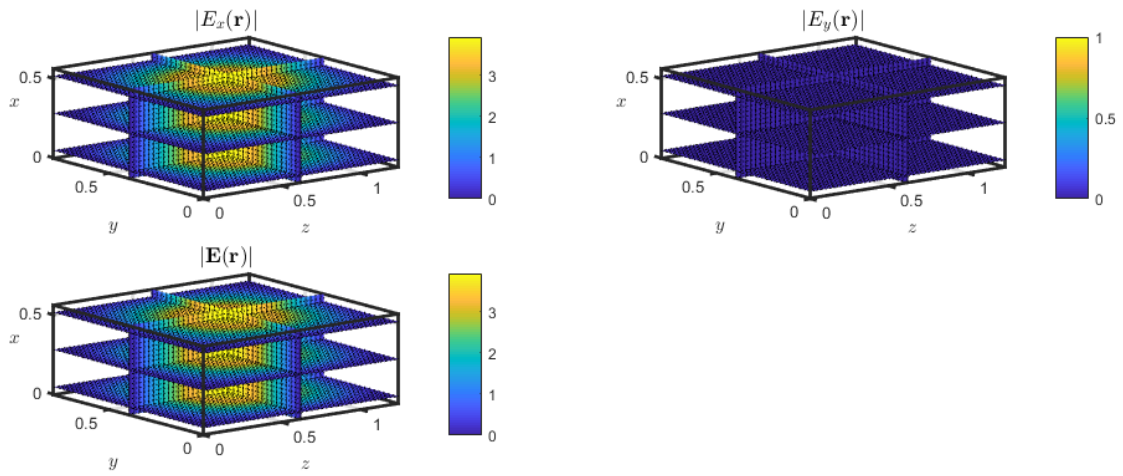

Fig. 3.5: Plot of $|E_x(\mathbf{r})|$, $|E_y(\mathbf{r})|$, and $|\mathbf{E}(\mathbf{r})|$ for the TE_{011} mode

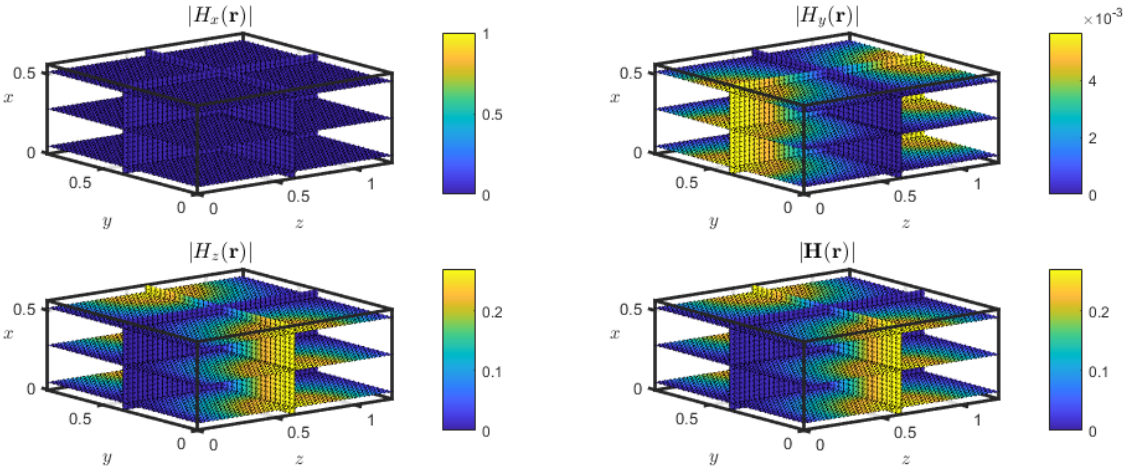

Fig. 3.6: Plot of $|H_x(\mathbf{r})|$, $|H_y(\mathbf{r})|$, $|H_z(\mathbf{r})|$, and $|\mathbf{H}(\mathbf{r})|$ for the TE_{011} mode

The electric field, solely consists of a x-component and is strongest at $(y, z) = (0.4, 0.625)$ for all values of x. The magnetic field has both, a y and z-component and, with the y-component being roughly two orders of magnitude less than the z-component, is at a maximum at $(y, z) = (0, 0.625)$ and $(y, z) = (0.8, 0.625)$ for all values of x.

3.5 Surface Currents

During the VPP, the PEBB undergoes thermal and mechanical optimization. These processes typically will consider cooling methods such as air cooling, water cooling, etc, which introduces the possibility of having ventilation slots or apertures. The placement of these slots or apertures can have a detrimental impact on the system by allowing radiation to leak out of the cavity. Therefore, it is desirable to select locations for these slots or apertures to be in regions where this effect is minimized. The surface current at each wall is given by

$$\mathbf{J}_{s_{ij}} = \hat{\mathbf{n}} \times \mathbf{H} \tag{3.122}$$

where $\hat{\mathbf{n}}$ is the unit vector normal to the $ij-$plane. Then, the surface currents for the TM^z modes are

$$\begin{aligned}\mathbf{J}_{s_{xz}} &= \hat{\mathbf{y}} \times \bigg(\frac{m_z\pi}{b} \sin\Big(\frac{n_z\pi x}{a}\Big) \cos\Big(\frac{m_z\pi y}{b}\Big) \cos\Big(\frac{p_z\pi z}{c}\Big)\hat{\mathbf{x}} \\ &\qquad - \frac{n_z\pi}{a} \cos\Big(\frac{n_z\pi x}{a}\Big) \sin\Big(\frac{m_z\pi y}{b}\Big) \cos\Big(\frac{p_z\pi z}{c}\Big)\hat{\mathbf{y}} \bigg) \\ &= -\frac{m_z\pi}{b} \sin\Big(\frac{n_z\pi x}{a}\Big) \cos\Big(\frac{m_z\pi y}{b}\Big) \cos\Big(\frac{p_z\pi z}{c}\Big)\hat{\mathbf{x}}\end{aligned} \tag{3.123}$$

$$\begin{aligned}\mathbf{J}_{s_{yz}} &= \hat{\mathbf{x}} \times \bigg(\frac{m_z\pi}{b} \sin\Big(\frac{n_z\pi x}{a}\Big) \cos\Big(\frac{m_z\pi y}{b}\Big) \cos\Big(\frac{p_z\pi z}{c}\Big)\hat{\mathbf{x}} \\ &\qquad - \frac{n_z\pi}{a} \cos\Big(\frac{n_z\pi x}{a}\Big) \sin\Big(\frac{m_z\pi y}{b}\Big) \cos\Big(\frac{p_z\pi z}{c}\Big)\hat{\mathbf{y}} \bigg) \\ &= -\frac{n_z\pi}{a} \cos\Big(\frac{n_z\pi x}{a}\Big) \sin\Big(\frac{m_z\pi y}{b}\Big) \cos\Big(\frac{p_z\pi z}{c}\Big)\hat{\mathbf{y}}\end{aligned} \tag{3.124}$$

$$\begin{aligned}\mathbf{J}_{s_{xy}} &= \hat{\mathbf{z}} \times \bigg(\frac{m_z\pi}{b} \sin\Big(\frac{n_z\pi x}{a}\Big) \cos\Big(\frac{m_z\pi y}{b}\Big) \cos\Big(\frac{p_z\pi z}{c}\Big)\hat{\mathbf{x}} \\ &\qquad - \frac{n_z\pi}{a} \cos\Big(\frac{n_z\pi x}{a}\Big) \sin\Big(\frac{m_z\pi y}{b}\Big) \cos\Big(\frac{p_z\pi z}{c}\Big)\hat{\mathbf{y}} \bigg) \\ &= \frac{n_z\pi}{a} \cos\Big(\frac{n_z\pi x}{a}\Big) \sin\Big(\frac{m_z\pi y}{b}\Big) \cos\Big(\frac{p_z\pi z}{c}\Big)\hat{\mathbf{x}} \\ &\quad + \frac{m_z\pi}{b} \sin\Big(\frac{n_z\pi x}{a}\Big) \cos\Big(\frac{m_z\pi y}{b}\Big) \cos\Big(\frac{p_z\pi z}{c}\Big)\hat{\mathbf{y}}\end{aligned} \tag{3.125}$$

and the surface currents for the TE^z modes are

$$\begin{aligned}
\mathbf{J}_{s_{xz}} = \hat{\mathbf{y}} \times \frac{i}{\omega\mu}\Bigg\{ & \frac{u_z w_z \pi^2}{ac} \sin\Big(\frac{u_z \pi x}{a}\Big) \cos\Big(\frac{v_z \pi y}{b}\Big) \cos\Big(\frac{w_z \pi z}{c}\Big)\hat{\mathbf{x}} \\
& + \frac{v_z w_z \pi^2}{bc} \cos\Big(\frac{u_z \pi x}{a}\Big) \sin\Big(\frac{v_z \pi y}{b}\Big) \cos\Big(\frac{w_z \pi z}{c}\Big)\hat{\mathbf{y}} \\
& + \left(\frac{w_z^2 \pi^2}{c^2} - k^2\right) \cos\Big(\frac{u_z \pi x}{a}\Big) \cos\Big(\frac{v_z \pi y}{b}\Big) \sin\Big(\frac{w_z \pi z}{c}\Big)\hat{\mathbf{z}} \Bigg\} \\
= \frac{i}{\omega\mu}\Bigg[& \left(\frac{w_z^2 \pi^2}{c^2} - k^2\right) \cos\Big(\frac{u_z \pi x}{a}\Big) \cos\Big(\frac{v_z \pi y}{b}\Big) \sin\Big(\frac{w_z \pi z}{c}\Big)\hat{\mathbf{x}} \\
& - \frac{u_z w_z \pi^2}{ac} \sin\Big(\frac{u_z \pi x}{a}\Big) \cos\Big(\frac{v_z \pi y}{b}\Big) \cos\Big(\frac{w_z \pi z}{c}\Big)\hat{\mathbf{z}} \Bigg]
\end{aligned} \tag{3.126}$$

$$\begin{aligned}
\mathbf{J}_{s_{yz}} = \hat{\mathbf{x}} \times \frac{i}{\omega\mu}\Bigg\{ & \frac{u_z w_z \pi^2}{ac} \sin\Big(\frac{u_z \pi x}{a}\Big) \cos\Big(\frac{v_z \pi y}{b}\Big) \cos\Big(\frac{w_z \pi z}{c}\Big)\hat{\mathbf{x}} \\
& + \frac{v_z w_z \pi^2}{bc} \cos\Big(\frac{u_z \pi x}{a}\Big) \sin\Big(\frac{v_z \pi y}{b}\Big) \cos\Big(\frac{w_z \pi z}{c}\Big)\hat{\mathbf{y}} \\
& + \left(\frac{w_z^2 \pi^2}{c^2} - k^2\right) \cos\Big(\frac{u_z \pi x}{a}\Big) \cos\Big(\frac{v_z \pi y}{b}\Big) \sin\Big(\frac{w_z \pi z}{c}\Big)\hat{\mathbf{z}} \Bigg\} \\
= \frac{i}{\omega\mu}\Bigg[& - \left(\frac{w_z^2 \pi^2}{c^2} - k^2\right) \cos\Big(\frac{u_z \pi x}{a}\Big) \cos\Big(\frac{v_z \pi y}{b}\Big) \sin\Big(\frac{w_z \pi z}{c}\Big)\hat{\mathbf{y}} \\
& + \frac{v_z w_z \pi^2}{bc} \cos\Big(\frac{u_z \pi x}{a}\Big) \sin\Big(\frac{v_z \pi y}{b}\Big) \cos\Big(\frac{w_z \pi z}{c}\Big)\hat{\mathbf{z}} \Bigg]
\end{aligned} \tag{3.127}$$

$$\begin{aligned}
\mathbf{J}_{s_{xy}} = \hat{\mathbf{z}} \times \frac{i}{\omega\mu}\Bigg\{ & \frac{u_z w_z \pi^2}{ac} \sin\Big(\frac{u_z \pi x}{a}\Big) \cos\Big(\frac{v_z \pi y}{b}\Big) \cos\Big(\frac{w_z \pi z}{c}\Big)\hat{\mathbf{x}} \\
& + \frac{v_z w_z \pi^2}{bc} \cos\Big(\frac{u_z \pi x}{a}\Big) \sin\Big(\frac{v_z \pi y}{b}\Big) \cos\Big(\frac{w_z \pi z}{c}\Big)\hat{\mathbf{y}} \\
& + \left(\frac{w_z^2 \pi^2}{c^2} - k^2\right) \cos\Big(\frac{u_z \pi x}{a}\Big) \cos\Big(\frac{v_z \pi y}{b}\Big) \sin\Big(\frac{w_z \pi z}{c}\Big)\hat{\mathbf{z}} \Bigg\} \\
= \frac{i}{\omega\mu}\Bigg[& - \frac{v_z w_z \pi^2}{bc} \cos\Big(\frac{u_z \pi x}{a}\Big) \sin\Big(\frac{v_z \pi y}{b}\Big) \cos\Big(\frac{w_z \pi z}{c}\Big)\hat{\mathbf{x}} \\
& + \frac{u_z w_z \pi^2}{ac} \sin\Big(\frac{u_z \pi x}{a}\Big) \cos\Big(\frac{v_z \pi y}{b}\Big) \cos\Big(\frac{w_z \pi z}{c}\Big)\hat{\mathbf{y}} \Bigg].
\end{aligned} \tag{3.128}$$

Plots of the surface currents at the cavity walls, obtained by equations 3.123-3.128, are shown below in Figure 3.7 for the TM_{110} mode and the TE_{011} mode.

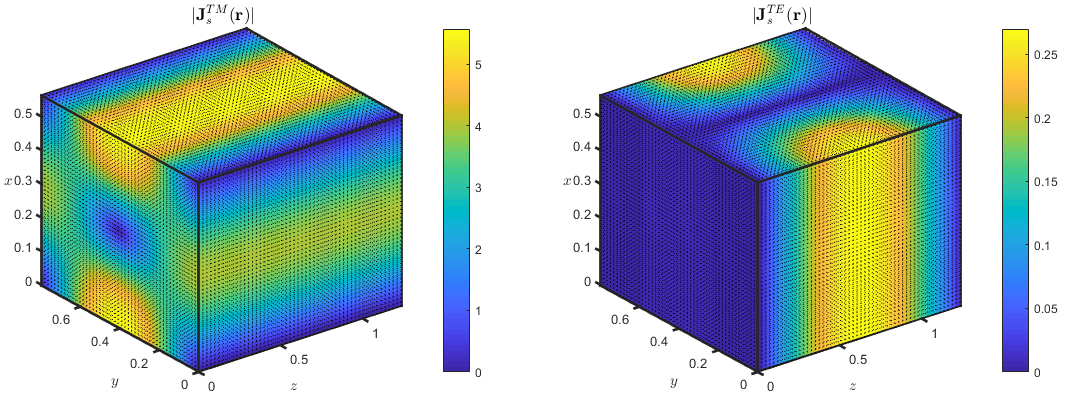

Fig. 3.7: Plot of $|J_s(\mathbf{r})|$ for the TM_{110} mode (left) and $|J_s(\mathbf{r})|$ for the TE_{011} mode (right)

Using this data, we are able to determine general locations where the radiation will be minimized if an aperture or slot is made in the cavity.

For example, the current on the upper cavity wall in the yz-plane for the TE_{011} shown above in Figure 3.7 is directed in the $\hat{\mathbf{u}} = \hat{\mathbf{y}} + \hat{\mathbf{z}}$ direction. Narrow ventilation slots placed in parallel with the direction of the current where the current is at a minimum will result in minimal radiation. On the other hand, placing a narrow ventilation slot perpendicular to the current, or in locations where the current is at a maximum, will result in significant radiation.

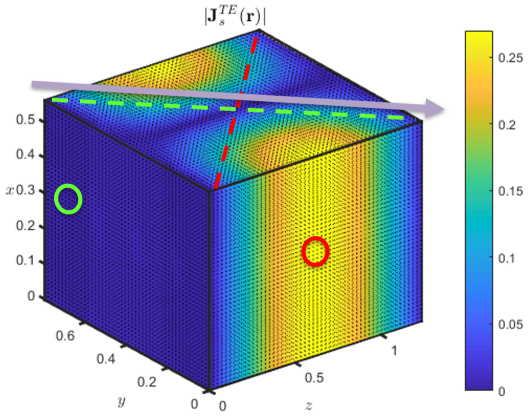

Fig. 3.8: Example of good and bad placement of a ventilation slot and aperture

This concept is depicted above in Figure 3.8. The arrow indicates the direction of the current, the green markings represent an example of good placement, and the red markings represent an example of bad placement.

THIS PAGE INTENTIONALLY LEFT BLANK

Chapter 4

Integration into the Virtual Prototyping Process

The mathematical formulation can be modeled through computational software and integrated into the VPP by considering the objective of removing any resonant modes created by the enclosure. The spectral location of the modes are dependent on the volume of the cavity, thus constraints on the volume of the cavity formed by the enclosure and the components, and subsequently the overall dimensions of the PEBB LRU must be derived in order to satisfy the objective. This chapter will present some possible approaches to integrating the high frequency model into the VPP and discuss how the constraints derived from these models can benefit the VPP.

4.1 Frequency-Objective-Based Constraints

Equations 3.88 and 3.113, shown below for reference,

$$f_{\mathrm{TM}} = \frac{1}{2\sqrt{\mu\varepsilon}}\sqrt{\left(\frac{n_i}{a}\right)^2 + \left(\frac{m_i}{b}\right)^2 + \left(\frac{p_i}{c}\right)^2}$$

$$f_{\mathrm{TE}} = \frac{1}{2\sqrt{\mu\varepsilon}}\sqrt{\left(\frac{u_i}{a}\right)^2 + \left(\frac{v_i}{b}\right)^2 + \left(\frac{w_i}{c}\right)^2}$$

enables one to determine the frequency at a which specific mode occurs for a given volume. For a rectangular cavity with $a \leq b \leq c$, dominant mode is the TE_{011} mode and this will be the main focus throughout this chapter. For other resonant modes, Table 4.1 [23] shows $(f_r)_{nmp}/(f_r)_{011}$ for $a \leq b \leq c$.

$\frac{b}{a}$	$\frac{c}{a}$	TE_{011}	TE_{101}	TM_{110}	$\frac{TM_{111}}{TE_{111}}$	TE_{012}	TE_{021}	TE_{201}	TE_{102}	TM_{120}	TM_{210}	$\frac{TM_{112}}{TE_{112}}$
1	1	1	1	1	1.22	1.58	1.58	1.58	1.58	1.58	1.58	1.73
1	2	1	1	1.26	1.34	1.26	1.84	1.84	1.26	2.00	2.00	1.55
2	2	1	1.58	1.58	1.73	1.58	1.58	2.91	2.00	2.00	2.91	2.12
2	4	1	1.84	2.00	2.05	1.26	1.84	3.60	2.00	2.53	3.68	2.19
4	4	1	2.91	2.91	3.00	1.58	1.58	5.71	3.16	3.16	5.71	3.24
4	8	1	3.62	3.65	3.66	1.26	1.84	7.20	3.65	4.03	7.25	3.82
4	16	1	3.88	4.00	4.01	1.08	1.96	7.76	3.91	4.35	7.83	4.13

Table 4.1: $(f_r)_{nmp}/(f_r)_{011}$ for a Rectangular Cavity, $a \leq b \leq c$ [23]

Note that all resonant modes associated with Table 4.1 are TE^z. The first approach is to derive constraints on the range of volumes by extracting volumes for which the TE_{011} exists above the frequency range of the switching harmonics. First, the initial limits, both upper and lower, on the length, width, and height and the dimensions of the PEBB assembly can be used to determine the limits which describe the cavity formed between the PEBB assembly and the enclosure. The difference between the limits should then be discretized according to a sample size which gives adequate resolution. The dimensions should then be converted into $N \times N \times N$ matrix in order to capture every possible cavity volume. In computational software such as MATLAB, this can accomplished through the use of the *meshgrid()* function. The dimensions are then used to create a three dimensional matrix $\mathbf{F}_{011}$ by using Equation 3.113, and will take the form of

$$\mathbf{F}_{011} = \frac{1}{2\sqrt{\mu\varepsilon}}\sqrt{\left(\frac{0}{\mathbf{A}}\right)^2 + \left(\frac{1}{\mathbf{B}}\right)^2 + \left(\frac{1}{\mathbf{C}}\right)^2}, \tag{4.1}$$

resulting in a three dimensional matrix, where each point within the matrix is the frequency

of the TE_{011} mode which corresponds to a specific length, width, and height within the range defined. Volumes which do not contain the TE_{011} within the frequency range of the switching harmonics can then be extracted out of the data by iterating through $\mathbf{F}_{011}$, selecting only the elements which have values larger than the greatest switching harmonic of interest.

4.2 Modal-Objective-Based Constraints

Another approach is to begin with determining the number of modes for a given frequency and then derive constraints on the volume. Liu, Chang, and Ma [24] have extensively studied the resonant frequencies of rectangular cavities and have determined the total number N of modes with eigenvalues k_{nmp} less than or equal to k by computer counting using equations 3.84 and 3.109. Although N as a function of k or f is discontinuous, they have also derived a smooth approximation N_s given by [24]

$$N_s(k) = \frac{abc}{3\pi^2}k^3 - \frac{a+b+c}{2\pi}k + \frac{1}{2} \qquad (k > 0), \tag{4.2}$$

or in terms of frequency f,

$$N_s(f) = \frac{8\pi}{3}abc\frac{f^3}{\nu^3} - (a+b+c)\frac{f}{\nu} + \frac{1}{2} \qquad (f > 0), \tag{4.3}$$

where $\nu = 1/\sqrt{\mu\varepsilon}$.

Equations 4.2 and 4.3 can be utilized in the VPP in two significant ways. Unlike the first approach, the harmonic content associated with a specified switching frequency, as well as the limits of the PEBB assembly dimensions which are required in order to create a design space which accounts for every possible length, width, and height are used as inputs. Then, for a specific frequency, a plot of all of the designs with $N < 1$ can be generated as shown below in Figure 4.1.

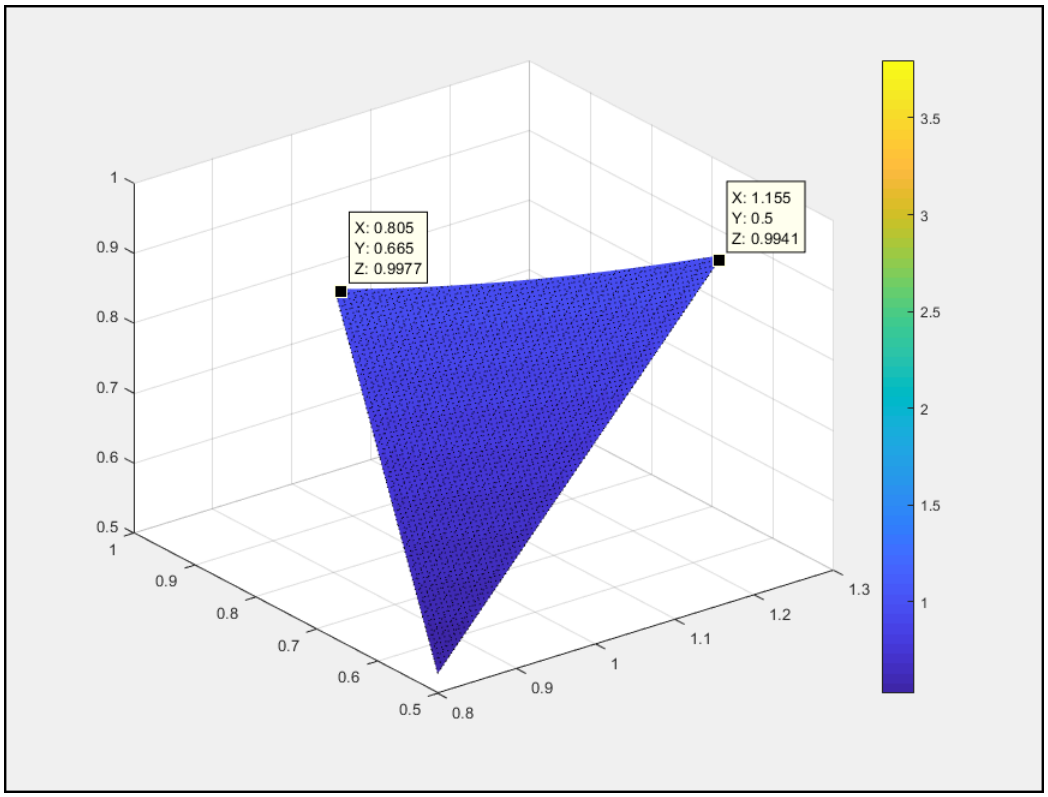

Fig. 4.1: Designs with $N < 1$ for $f = 220$ MHz

While the results are similar to the first approach, in the sense that constraints on the volume are derived from a frequency, this approach can also be used to derive constraints on the switching frequency. Spectral decomposition can be performed for a given switching frequency and the resulting harmonics can be input into this model, yielding a set of volumes for which the number of modes are less than 1, i.e., non-existent. This enables the VPP investigate the feasibility of various switching frequencies and its impact on volume, as well as the switching capabilities of WBG devices.

4.3 Constraints on the Layout of the PEBB

While incorporating a near-field analysis on the PEBB assembly within the VPP is not feasible, the assumptions made in this work, in regards to the layout of the assemblies within the PEBB LRU, provide a baseline for which the high frequency effects can be captured and integrated into the VPP. The calculation of the surface currents at the cavity walls

can be incorporated into the VPP, providing constraints on the placement of ventilation holes or apertures while providing additional information to the selection of a thermal management system. Once a optimal design is achieved, one could then fine tune the layout using electromagnetic modeling software by investigating various components of differing geometries. Furthermore, the constraints on the volume derived above provide a baseline for which the PEBB assembly should be laid out to avoid resonances.

The resonant modes associated with a rectangular cavity, whose height a, width b, and length c are such that $a \leq b \leq c$, are highly dependent on variations in width and length and seemingly invariant on variations in height. Since the height a is taken in this formulation to be the distance between the PEBB assembly and the enclosure, layout decisions which impact the length and width of the PEBB assembly drive any resonances which may exist in the main cavity of the PEBB LRU. Not only does the constraints derived on the length and width of the PEBB assembly provide insight on the layout, but it also provides additional constraints on the method of cooling, i.e., thermal management systems, allocations for dielectric stand-off distances, accessibility, and frame support, interconnections, cabling, capacitor sizes, and bus bar designs. These constraints, informed by the LRU level, can be used to identify genes which can be used in a VPP to determine the optimal placement of components, spacing between components, and placement of apertures or slots for ventilation for a given design.

THIS PAGE INTENTIONALLY LEFT BLANK

Chapter 5

Conclusion and Future Works

The value proposition of WBG devices have yet to be realized in their application to power electronic converters due to the trade-off between exploiting their full switching capabilities and the generation of EMI. The VPP approach [18], which incorporates the high frequency effects of WBG devices into the metamodel generation process, provides the means to comprehensively investigate these trade-offs within the framework of the United States Navy's platform for ship design, S3D. A mathematical model which captures the radiated high frequency effects of WBG devices for the PEBB LRU was formulated in this work.

The constraints derived in this work, while only a starting point, will be used to incorporate radiated high frequency effects into the metamodeling approach via the VPP and provide a baseline for the development of PEBB assemblies through volumetric constraints on the layout. Future works include developing a VPP for the PEBB LRU, the incorporation of near-field measurements into the VPP using approaches such as [25], and investigating the effects of higher switching frequencies and resonances within the framework of this thesis for low voltage systems. The use of near-field measurements will refine the VPP for the PEBB LRU, which is built upon this work, and will enable more detailed designs to be investigated through the VPP. For low voltage systems which do not have constraints on switching frequency, the VPP can obtain a set of designs for which the dominant mode has been eliminated at higher switching frequencies, thus enabling a method of determining the value of WBG devices in low voltage systems or the associated trade-offs.

THIS PAGE INTENTIONALLY LEFT BLANK

References

Cited References

[1] F. Wang et al. "Advances in Power Conversion and Drives for Shipboard Systems". In: *Proceedings of the IEEE*. Vol. 103. 12. Dec. 2015, pp. 2285–2311.

[2] X. She et al. "Review of Silicon Carbide Power Devices and Their Applications". In: *IEEE Trans. Ind. Electron.* 64.10 (Oct. 2017), pp. 8193–8205.

[3] P. Roussel. "SiC market and industry update". In: *Int. SiC Power Electron. Appl. Workshop*. Kista, Sweeden, 2011.

[4] J. Millan et al. "A Survey of Wide Bandgap Power Semiconductor Devices". In: *IEEE Trans. Power Electron.* 29.5 (May 2014), pp. 2155–2163.

[5] J. Richmond. *Hard-Switched Silicon IGBTs? Cut Switching Losses in Half with Silicon Carbide Schottky Diodes*. URL: `http://www.richardsonrfpd.com/resources/RellDocuments/SYS_31/Wlf_Hard_Switched.pdf`.

[6] F. Zare et al. "Electromagnetic Interference Issues of Power Electronics Systems with Wide Band Gap Semiconductor Devices". In: *IEEE Energy Conversion Congress and Exposition (ECCE)*. 2015, pp. 5946–5951.

[7] D. Han et al. "Comparative Analysis on Conducted CM EMI Emissions of Motor Drives: WBG Versus Si Devices". In: *IEEE Trans. Ind. Electron.* 64.10 (Oct. 2017), pp. 8353–8363.

[8] N. Oswald et al. "An Experimental Investigation of the Tradeoff between Switching Losses and EMI Generation With Hard-Switched All-Si, Si-SiC, and All SiC Device Combinations". In: *IEEE Trans. Power Electron.* 29.5 (May 2014), pp. 2393–2407.

[9] X. Chen et al. "An Advanced Design of Power Module with EMI Reduction Method". In: *IEEE Energy Conversion Congress and Exposition (ECCE)*. 2018, pp. 4671–4674.

[10] C. DiMarino et al. "A Higher-Power-Density, High-Speed Gate Driver for a 10 kV SiC MOSFET Module". In: *IEEE Electric Ship Technologies Symposium (ESTS)*. 2017, pp. 629–634.

[11] C. DiMarino et al. "10 kV, 120 A SiC MOSFET Modules for a Power Electronics Building Block (PEBB)". In: *IEEE Workshop on Wide Bandgap Power Devices and Applications*. 2014, pp. 55–58.

[12] C. DiMarino et al. "A Wire-bond-less 10 kV SiC MOSFET Power Module with Reduced Common-mode Noise and Electric Field". In: *PCIM Europe 2018; Intl. Exhib. and Conf. for Power Electron., Intell. Motion, Renewable Energy and Energy Manag.* Nuremberg, Germany, 2018.

[13] R. Cuzner et al. “Power converter metamodeling approach for the smart ship design environment”. In: *IEEE Electric Ship Technologies Symposium (ESTS)*. 2017, pp. 118–125.

[14] R. Cuzner et al. “Approach to Scalable Model Development for Navy Shipboard Compatible Modular Multilevel Converters”. In: *IEEE Trans. Emerg. Sel. Topics Power Electron.* 5 (Mar. 2017), pp. 28–39.

[15] S. D. Sudhoff and G. M. Shane. “Metamodeling of rotating electric machinery”. In: *IEEE Trans. Energy Convers.* (2018).

[16] S. D. Sudhoff, G. M. Shane, and H. Suryanarayana. “Magnetic-equivalent-circuit-based scanling laws for low-frequency magnetic devices”. In: *IEEE Trans. Energy Convers.* 28.3 (2018), pp. 746–755.

[17] R. Cuzner and R. Siddaiah. “Derivation of Power System Module Metalmodels for Early Shipboard Design Explorations”.

[18] R. Cuzner, R. Siddaiah, and T. Nguyen. “Applying a Virtual Protoyping Process to Generate Pareto Optimal Solutions for a Modular Multi-Level MVAC to MVDC Converter”.

[19] S. D. Sudhoff. *Power Magnetic Devices: A Multi-Objective Design Approach*. Ed. by M. E. El-Hawary. Wiley, 2014.

[20] R. M. Burkart. “Advanced Modeling and Multi-Objective Optimization of Power Electronic Converter Systems”. PhD thesis. ETH Zurich, 2016.

[21] J. Wang et al. “Design and Testing of 6 kV H-bridge Power Electronics Building Block Based on 10 kV SiC MOSFET Module”. In: *2018 International Power Electronics Conference (IPEC-Niigata 2018 -ECCE Asia)*. 2018, pp. 3985–3992.

[22] J. Wang et al. “Power Electronics Building block (PEBB) design based on 1.7 kV SiC MOSFET modules”. In: *IEEE Electric Ship Technologies Symposium (ESTS)*. 2017, pp. 612–619.

[23] R. F. Harrington. *Time-Harmonic Electromagnetic Fields*. Ed. by D. G. Dudley. Wiley-Interscience, 2001.

[24] B. H. Liu, D. C. Chang, and M. T. Ma. *Eigenmodes and the composite quality factor of a reverberating chamber*. U.S. Nat. Bur. Stand. Tech. Note 1066. 1983.

[25] P. Li et al. “A DGTD Scheme for Modeling the Radiated Emission From DUTs in Shielding Enclosures Using Near Electric Field Only”. In: *IEEE Trans. Electromagn. Compat.* 58.2 (2016), pp. 457–467.

Related References

C. DiMarino et al. “Design of a novel, high-density 10 kV SiC MOSFET Module”. In: *IEEE Energy Conversion Congress and Exposition (ECCE)*. 2017, pp. 4000–4010.

A. Hefner et al. “Recent Advances in High-Voltage, High-Frequency Silicon-Carbide Power Devices”. In: *Conf. Rec. IEEE Ind. Appl. Conf.* Oct. 2006, pp. 330–337.

R. M. Burkart and J. W. Kolar. “Comparative $\eta - \rho - \sigma$ Pareto Optimization of Si and SiC Multilevel Dual-active-bridge topologies with wide input voltage range”. In: *IEEE Trans. Power Electron.* 32.7 (July 2017), pp. 5258–5270.

R. M. Burkart and J. W. Kolar. "Comparative evaluation of SiC and Si PV inverter systems based on power density and efficiency as indicators of initial cost and operating revenue". In: *2013 IEEE 14th Workshop on Control and Modeling for Power Electronics (COMPEL)*. 2013, pp. 1–6.

Y. Xu et al. "Electrical Field Analysis and Insulation Evaluation of a 6 kV H-bridge Power Electronics Building Block (PEBB) using 10 kV SiC MOSFET Devices". In: *IEEE Energy Conversion Congress and Exposition (ECCE)*. 2018, pp. 2428–2435.

B. J. Baliga. *Silicon Carbide Power Devices*. World Scientific Publishing, 2006.

B. J. Baliga. *Fundamentals of Power Semiconductor Devices*. Springer, 2008.

D. A. Hill. *Electromagnetic Fields in Cavities: Deterministic and Statistical Theories*. Wiley, 2009.

D. Griffiths. *Introduction to Electrodynamics*. 4th ed. Cambridge University Press, 2017.